KU LEUVEN

FACULTY OF SCIENCE

Parameter Estimation with LISA's Correlated Noise

Karel PLETS

Supervisor: Prof. Alvin J.K. Chua
Affiliation *National University of Singapore*

Cosupervisor: *Prof. Tjonnie G.F. Li*
Affiliation *KU Leuven*

Mentor: *Simon Maenaut*
Affiliation *KU Leuven*

Master thesis submitted in fulfillment of the requirements for the degree in Master of Science in Physics

Academic year 2024-2025

Preface

When last year I had received the opportunity to go on exchange to the National University of Singapore (NUS), I was quite ecstatic. Not only had I gotten the chance to study and learn about the Singaporean way of higher education, but I also hoped to collaborate with the physics team in NUS by creating a joint thesis project. It was then with great pleasure to suggest my own project under supervision of professors Alvin Chua and Tjonnie Li. In retrospective of the past year, I can only look back with gratitude. While my results did not turn out to be the ideal and I received some unexpected turns, I am still rather happy to have chosen this project as a final send-off for my now 5 year long journey at KU Leuven, as to say. As you will likely agree, I did not make it easy for myself or choose the best topic, so I am nevertheless rather satisfied with the results I have come up with, in spite of the setbacks and not reaching the initial end goal. Hoping to continue and further my career in academia, it seems likely to me I will be leaving my hometown onto other cities and countries to grow my skills and hopefully start a doctoral programme.

I would like to first thank prof. Alvin Chua and Tjonnie Li for their support and ability to get this joint project rolling. Aside from their valuable input and technical insights, they have also been great mentors in my academic journey and made fine promotors. Furthermore, I would like to thank soon-to-be Doctor Simon Maenaut for his daily supervision during my thesis project as well as his guidance, mentorship and friendship before the start of my thesis. I could not be happier to have had him for my thesis in his own final year of his PhD in spite of the lack of truly overlapping expertises. In that regard, I would also like to thank Milan Wils and Francesco Cireddu for their advice and help with understanding the theory *above the noise*.

Furthermore, I would like to thank my uncle[1] Hans Plets for his support during my thesis journey and for first introducing me to the world and potential of gravitational wave physics. It probably would not have been without him that I ended up in this area of research.

Finally, I would also like to thank all of my friends and colleagues Bert Depoorter, Alexander Arutunyan, Sheena Abigail and August Vannes who supported me throughout the year and read through my thesis whilst I was finishing it up. Their advice and comments were genuinely valuable and well-appreciated as I was finishing everything up in the hours leading up to the submission deadline. I would like to emphasise the help Bert was able to provide me in Leuven as well as while I was in Singapore, both in discussing our relatively similar thesis topics, and in being everyone's *technical support*, whether or not he accepts the title.

[1]also known as *Nonkel Hans*

Summary

Among fields in high energy astrophysics, interest and research into gravitational waves (GWs) have been increasing significantly over the last few years since the LIGO discovery in 2015. In order to expand our understanding of this field, several proposals have been made for the next generation of GW detectors, such as the Einstein Telescope (ET) and the Laser Interferometer Space Antenna (LISA). Recently, research by Cireddu et collaborators found that taking correlated noise into account can improve the parameter estimation. While this work was performed for ET and symmetric noise, a similar analysis has yet to be made for the expected asymmetric noise LISA is expected to have. The presented master of physics thesis project attempts to asses the effects produced by the noise asymmetry through the comparison of the signal-to-noise ratio as well as quantifying the uncertainties through fisher information matrices and full parameter estimation. While not fully succeeding at the latter, the process of the attempt is discussed in detail and future avenues to reach this ideal have been shared.

Glossary

A_{ij} The TM noise parameter for the single-link detector going from spacecraft i to spacecraft j.

AU Astronomical Unit: Unit of distance defined as the average distance between the Earth and the Sun.

$\Gamma^{\mu}_{\alpha\beta}$ The Christoffel symbols, defined as $\Gamma^{\mu}_{\alpha\beta} = \frac{1}{2}g^{\mu\nu}(\partial_{\alpha}g_{\nu\beta} + \partial_{\beta}g_{\alpha\nu} - \partial_{\nu}g_{\alpha\beta})$. This is a coordinate-dependent measure for the curvature of a metric.

d_L Distance between the GW detector and the detected event, often used in GW cosmology.

G The Newtonian gravitational constant: $\sim 6.67 \times 10^{-11}\ \mathrm{m}^3 \cdot \mathrm{kg}^{-1} \cdot \mathrm{s}^{-2}$.

Hz Hertz.

km Kilometer.

c The speed of light: $\sim 2.997 \times 10^8\ \mathrm{m} \cdot \mathrm{s}^{-1}$.

ls a lightsecond, i.e. the distance travelled by light in a vaccuum in one second: $1\ \mathrm{ls} = c \cdot (1\ \mathrm{s}) \approx 2.997 \times 10^8\ \mathrm{m}$.

$\mathcal{M}_c$ The chirp mass: an often used parameter in GW binaries with units of mass. It can be derived from the individual binary masses m_1 and m_2 through the identity: $\mathcal{M}_c = (m_1 m_2)^{3/5}/(m_1 + m_2)^{1/5}$.

P_{ij} The OMS noise parameter for the single-link detector going from spacecraft i to spacecraft j.

Acronyms

BH Black Hole.

CBC Compact Binary Collisions.

CMB Cosmic Microwave Background.

CPU Central Processing Unit.

CSD Cross Power Spectral Density.

EFE Einstein Field Equations.

EM Electromagnetism.

EMR Euregion Meuse Rhine.

EMRI Extreme-Mass Ratio Inspiral.

ESA European Space Agency.

ET Einstein Telescope.

FFT Fast Fourier Transform.

FIM Fisher Information Matrix.

GB Galactic Binary.

GPU Graphical Processing Unit.

GR General Relativity.

GW Gravitational Waves.

HPC High-Performance Computing.

KAGRA Kamioka Gravitational Wave Detector.

LIGO Laser Interferometer Gravitational-Wave Observatories.

LISA Laser Interferometry Space Anthenna.

LLF Local Lorentz Frame.

LVK LIGO-Virgo-KAGRA.

MBHB Massive Black Hole Binary.

MCMC Markov Chain Monte Carlo.

ML Machine Learning.

NASA National Aeronautics and Space Administration.

NS Neutron Star.

OMS Optical Metrology Systems.

OOM Out of Memory.

PE Parameter Estimation.

PSD Power Spectral Density.

PTA Pulsar Timing Array.

SGWB Stochastic Gravitational Wave Background.

SMBH Supermassive Black Hole.

SN Supernova.

SNR Signal-to-Noise Ratio.

SSB Solar system's barycentric.

TDI Time-Delay Interferometry.

TM Test Mass.

TPU Tensor Processing Unit.

WD White Dwarf.

List of Figures

List of Tables

Contents

Chapter 1

Introduction: Theory and Motivation

Spacetime tells matter how to move; matter tells spacetime how to curve.

- John Archibald Wheeler, Geons, Black Holes and Quantum Foam: A Life in Physics

In this introduction, all the necessary theory will be discussed for the uninitiated reader. However, even though a short introduction to General Relativity (GR) and Gravitational Waves (GW) will be provided, a basic understanding in the (mathematics of) relativity will be assumed henceforth. Since the focus of this project is more in the noise and data analysis of the GW detectors, the focus will be put on understanding these aspects of the master thesis project.

1.1 Gravitational Waves

In GR, we no longer speak of space, time and gravity as all separate concepts, but all as interlinked. As stated by the quote in the beginning of this chapter, the distribution of matter and energy distorts spacetime, creating a curved 4D geometric space. In turn, the curved spacetime redefines the geometry of the system, giving a new meaning to distance and what constitutes a straight line. In a more exact sense, in order to mathematically describe the geometry of a physical system, the spacetime metric $g_{\mu\nu}$ is used, which allows us to actually calculate the distance and spacetime interval (otherwise known as the proper time) according to some specified coordinate system. However, since $g_{\mu\nu}$ is by definition very dependent on its coordinate system, we describe the curvature by other geometric objects, such as the Riemann tensor $R^{\mu}_{\nu\rho\sigma}$ and other quantities derived from it.[1]

According to GR (Maggiore (2017); Li (2024)), the geometry of a physical system can be linked to its gravity and matter by the Einstein Field Equations (EFE):

$$G_{\mu\nu} \equiv R_{\mu\nu} - \frac{1}{2}Rg_{\mu\nu} = \frac{8\pi G_N}{c^4}T_{\mu\nu}. \tag{1.1}$$

[1]such examples include: the Ricci tensor $R_{\mu\nu} = R^{\alpha}_{\mu\alpha\nu}$, the Ricci scalar $R = g^{\mu\nu}R_{\mu\nu}$ and the Einstein tensor $G_{\mu\nu} \equiv R_{\mu\nu} - \frac{1}{2}Rg_{\mu\nu}$.

Here, the Ricci tensor $R_{\mu\nu}$, the Ricci scalar R, the Einstein tensor $G_{\mu\nu}$ and the spacetime metric all describe the geometrical aspects of a physical system whereas the stress-energy tensor $T_{\mu\nu}$ describes the distribution of mass, energy and momentum across the system.

Quickly after the discovery of GR, Albert Einstein also predicted the existence of GWs as linear perturbations on spacetime.

Mathematically speaking, we can describe GWs as a perturbation on our metric:

$$g_{\mu\nu} \approx \eta_{\mu\nu} + h_{\mu\nu}, \tag{1.2}$$

where we state that $\eta_{\mu\nu} = \mathrm{diag}(-1, +1, +1, +1)$[2] is the Minkowski metric which describes flat spacetime, and $|h_{\mu\nu}| \ll 1$ is our perturbation, otherwise known as the GW. Similar to mechanical and electromagnetic waves, GWs can also be described by their own wave equation, called the linearised Einstein field equations (Maggiore (2017); Li (2024)):

$$\Box \bar{h}_{\mu\nu} = -\frac{16\pi G_N}{c^4} T_{\mu\nu}, \tag{1.3}$$

where $\Box = \eta_{\mu\nu}\partial^\mu\partial^\nu = -(1/c^2)\partial_t^2 + \nabla^2$ is the d'Alembertian and $\bar{h}_{\mu\nu}$ is the metric perturbation $h_{\mu\nu}$ under the harmonic gauge.[3](Maggiore (2017)) Notably, there are a few ways in which GWs differ from other waves like EM or mechanical waves. Due to the fact they are described by a 2-tensor, they have different polarisation modes from other transverse waves like electromagnetic waves. As opposed to linear or circular polarisations of light, $h_{\mu\nu}$ has 2 commonly used possible polarisations: the plus ($+$) and cross ($\times$) polarisations, which can be described as follows.
For a GW moving in the $z-$direction, the metric perturbation can generally be written as:(Maggiore (2017))

$$h_{ab}^{\mathrm{TT}}(t, z) = \begin{pmatrix} h_+ & h_\times \\ h_\times & -h_+ \end{pmatrix}_{ab} \cos(\omega(t - z/c)), \tag{1.4}$$

with h_+ ($h_\times$) the plus (cross) polarisation amplitudes of the wave and h_{ab}^{TT} the metric perturbation in the traceless-transverse gauge.[4] Alternatively, this can be written in terms of the spacetime interval ds^2:

$$\begin{aligned} \mathrm{d}s^2 = &- c^2\mathrm{d}t^2 + \mathrm{d}z^2 + (1 + h_+ \cos[\omega(t - z/c)])\mathrm{d}x^2 \\ &+ (1 - h_+ \cos[\omega(t - z/c)])\mathrm{d}y^2 + 2h_\times \cos[\omega(t - z/c)]\mathrm{d}x\mathrm{d}y. \end{aligned} \tag{1.5}$$

This can furthermore be visualised by figure 1.1

Finally, we can discuss the way by which GWs are measured. Due to the coordinate dependence among other reasons, the spacetime metric can never be measured directly. In order

[2]This particular convention for the Minkowski metric is also known as the 'mostly plus' convention and will remain the convention used for the rest of this thesis.

[3]The harmonic gauge is a certain gauge which stipulates that $\partial^\mu \bar{h}_{\mu\nu} = 0$.

[4]This gauge is a special case of the harmonic gauge and stipulates further that $h^{0\mu} = 0$ (i.e. transverse), and $h_i^i = 0$ (i.e. traceless).

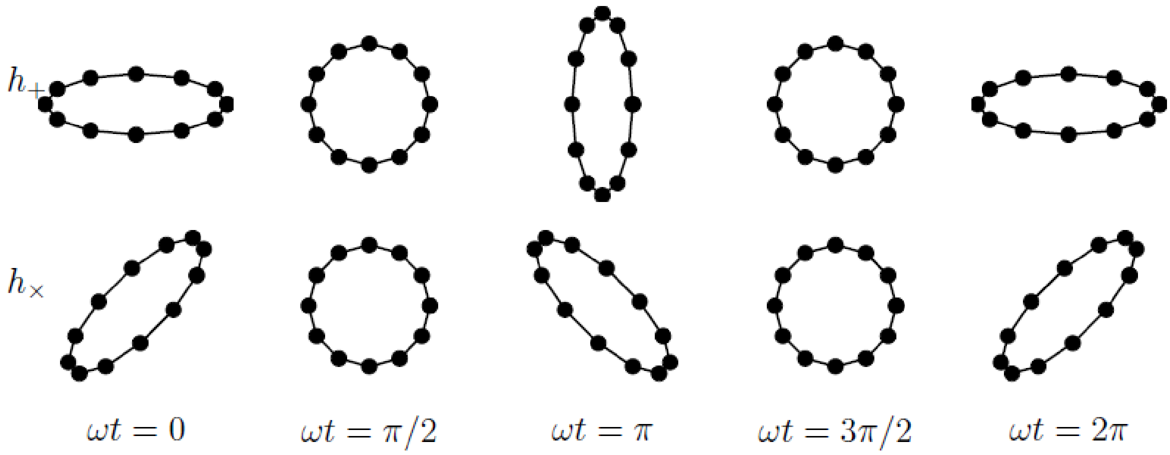

Figure 1.1: Visualisation demonstrating both the + and × polarisations, taken from (Li (2024))

to then detect GWs, we attempt to detect the small difference in distance when a GW passes through, with a scalar measure called the strain h. This quantity is defined as follows:

$$y(t) \equiv \frac{\Delta L}{L_0} = \frac{L(t) - L_0}{L_0}, \tag{1.6}$$

where we define ΔL as the armlength difference between the rest armlength L_0 and the time-dependent armlength $L(t)$ as a GW is passing through. This strain can be derived the following way, based on (Li (2024); Maggiore (2017)).

First note the fact light travels along null geodesics. Using equation (1.5), we therefore find that for our photon travelling solely along the $x-$axis ($y = z = 0$), its path equation obeys

$$\mathrm{d}s^2 = 0 = -c^2\mathrm{d}t^2 + (1 + h_+ \cos[\omega(t - z/c)])\mathrm{d}x^2 \tag{1.7}$$

or more simply after taking to the first order of $h_{\mu\nu}$,

$$\mathrm{d}x = \pm \mathrm{d}t \left(1 - \frac{1}{2}h_+ \cos(\omega t)\right). \tag{1.8}$$

Suppose you now have a light detector located on the $x-$axis from the origin to coordinate point x_1 such that when there is no passing GW ($h_+ = h_\times = 0$), the distance light takes from 1 end to the other is L_0, i.e. $L_0 \equiv \int_0^{x_1} \mathrm{d}x = c\int_0^t \mathrm{d}t'$, with $t - 0$ the time for the photon to travel from the origin to the end of the arm.
Now when a GW passes through, we find for our new armlength to be:

$$L(t) \equiv \int_0^{x_1} \mathrm{d}x = c\int_0^t \left(1 - \frac{1}{2}h_+ \cos(\omega t')\right)\mathrm{d}t' = L_0 - \frac{1}{2\omega}h_+ \sin(\omega t). \tag{1.9}$$

This then finally gives us the desired strain for a simple monochromatic GW:

$$y(t) = -\frac{c}{2\omega L_0}h_+ \sin(\omega t). \tag{1.10}$$

Note also how the contribution of the cross polarisation $h_\times$ is irrelevant for the strain. This will become important later when we discuss the various interferometers as the sky location of the GW compared to the orientation of the detector. We can generally find the observed strain to be a linear combination of strains caused by each polarisation term (Li (2024)):

$$y(t) = F_+ y_+(t) + F_\times y_\times(t), \tag{1.11}$$

where F_+ and $F_\times$ are called the antenna patterns and y_+, $y_\times$ the strain caused by the respective polarisation. These can be derived from its corresponding deformation $H(\mathbf{x}(\lambda), t(\lambda))$ by a GW:(Katz et al. (2022); Bayle (2019))

$$H(\vec{x}(\lambda), t(\lambda)) = F_+(\lambda) h_+(\lambda) + F_\times(\lambda) h_\times(\lambda) \tag{1.12}$$

which one can use to calculate $y(t)$ throughout a detector arm with the following relation:

$$y(t_i) = \frac{c}{2L(t_i)} \int_0^{L(t_i)} H(\vec{x}(\lambda), t(\lambda)) \mathrm{d}\lambda. \tag{1.13}$$

In general, F_+ and $F_\times$ are unitless time-dependent functions are they depend on the orientation of the detector which for certain detectors can change over time. For most short-time signals detected by ground-based detectors can assume stationarity, making F_+ and $F_\times$ constant. However, as will be shown later, the time-dependence of the antenna pattern becomes of huge importance for space-based detectors and one of the major differences with the current and future ground-based telescopes.(Bayle (2019))

1.2 GW Detectors

Currently, all viable GW detectors are various types of interferometers. Throughout this section, several currently-used and future detectors will be discussed and their inner workings. Furthermore, an illustration of a simple Michelson interferometer will first be discussed for illustration. As equation (1.10) also demonstrates for even simple formulations of interferometers, the detectable frequency range is inversely proportional to the detector's armlength for a constant sensitivity. For this reason, different detectors will have armlengths of different length scales so that different GW sources with other frequency ranges can be probed.

Ground-based detectors are usually limited to detector arm's on the order of $\sim 10^0$ to $\sim 5\times10^1$ kilometers that then gives one a detectable frequency range between $\sim 10^0$ and $\sim 10^5$ Hz.(Li (2024); Abac et al. (2025)) Space-based detectors massively increase the distance between the arms, on the order of ~ 8.33 ls[5], allowing us to probe the sub- Hz frequency range until $\sim 10^{-4}$ Hz.(Colpi et al. (2024); Tinto and Dhurandhar (2021)) Finally, there is the Pulsar Timing Array (PTA), which utilises the very consistent pulses of various millisecond pulsars to probe the lowest possible frequencies. PTAs then become a set of single-link interferometers with effective armlengths on the order of several lightyears and corresponding detectable range from 10^{-9} to 10^{-7} Hz.(Arzoumanian et al. (2020))

[5] or roughly $\sim 2.5 \times 10^6$ km

In spite of the ideal world we have thus far illustrated, any measurement comes with a lot of messy noise. This is even more the case in processing signals, where modelling the errors (i.e. the noise modelling) becomes an essential part of the analysis. The detectability of one signal can be properly quantified through the Signal-to-Noise Ratio (SNR). As the name implies, one can physically interpret this as the ratio between the power of the signal P_S (which is proportional to its square amplitude) to the average power of the expected noise P_N:(Li (2024))

$$\mathrm{SNR} \sim \frac{P_S}{P_N}. \tag{1.14}$$

A more formal and detailed introduction to the signal processing and data analysis is provided in section 1.3. Nonetheless, one can intuit that a signal becomes undetectable when $\mathrm{SNR} \lesssim 1$, and loud and detectable when $\mathrm{SNR} \gg 1$. When performing the data analysis or calculating the SNR, the detectability and Parameter Estimation (PE) of a signal can be improved in case a network of detectors as opposed to a singular detector is employed. This network's noise ought to be modelled with their total cumulative noise in mind. For GWs, each single detector can be expected to produce noise which, for each frequency, follows a Gaussian probability distribution centered at 0 and with a modelled variance. This variance at each frequency is called the Power Spectral Density (PSD).(Cireddu et al. (2024); Wong et al. (2024)) In certain cases, each detector's noise might be correlated with others and therefore a new measure named the Cross Power Spectral Density (CSD) is also employed, which may contain imaginary components. Physically, the CSD ought to be interpreted as the covariance of the noise between detectors at each frequency, analogous to imagining the PSD as the variance of a single detector's noise.(Cireddu et al. (2024)) As will be explained in section 1.3, these detectors form a covariance matrix with which the data analysis can finally be performed.

A simple Michelson Interferometer

Essentially, a Michelson inteferometer can be simplified as an L-shaped device with a mirror at the end of both arms and a laser emitter, beam splitter and photodetector. First, the laser shoots (monochromatic) light toward a beam splitter which reflects half of the beams and lets the other half pass through, respectively going in the direction of either arm. These beams then finally reflected by 2 respective mirrors that return each beam to each other, causing them to interfere with each other which is detected by the photodetector.

More exactly, we can model a simple Michelson interferometer with basic knowledge of optics, based on (Li (2024)). Suppose each arm is on the $x-$axis We can model the light beams as classical electrical fields. The input laser beam then becomes a monochromatic electric wave with wavenumber $\mathbf{k}$ and (angular) frequency ω_L:

$$E_{\mathrm{inp}} = E_0 e^{-i\omega_L t + i\mathbf{k}\cdot\mathbf{x}} \tag{1.15}$$

As a light beam hits a mirror, some part will also be reflected and another part will pass through. The proportion of reflected and transmitted beams can be quantified by its reflectivity (r_{mir}) and transmissivity (t_{mir}), defined as:

$$r_{\mathrm{mirr}} = \frac{E_{\mathrm{refl}}}{E_{\mathrm{inc}}}, \qquad t_{\mathrm{mirr}} = \frac{E_{\mathrm{trans}}}{E_{\mathrm{inc}}}, \tag{1.16}$$

with E_{refl}, E_{trans}, and E_{inc} the electric field of the reflected, transmitted and incoming beam, respectively. Furthermore, for an ideal mirror, we can assume energy conservation, which implies $1 = |r_{\text{mirr}}|^2 + |t_{\text{mirr}}|^2$. Finally, note also that for an electromagnetic wave coming from the other side of the mirror, it will have a reflectivity $r'_{\text{mirr}} = -r_{\text{mirr}}$ and transmissivity $t'_{\text{mirr}} = -t_{\text{mirr}}$.

In a perfect beam splitter, we can assume equal reflectivity and transmissivity: $r_{\text{BS}} = t_{\text{BS}} = 1/\sqrt{2}$. After hitting the beam splitter, the laser appropriately is split into a symmetric and anti-symmetric beam, the latter of which is measured by the photodetector. A simple derivation will then allow you to find that the respective symmetric (E_{sym}) and anti-symmetric (E_{ant}) beams produce the following electric fields:

$$E_{\text{sym}} = \frac{1}{2} E_{\text{inp}} e^{-2ikL} \left(r_x e^{ik\delta} + r_y e^{-ik\delta} \right), \tag{1.17}$$

$$E_{\text{ant}} = \frac{1}{2} E_{\text{inp}} e^{-2ikL} \left(r_x e^{ik\delta} - r_y e^{-ik\delta} \right). \tag{1.18}$$

Here, $L = L_x + L_y$ is the average between the (mean) distance of both arms, r_x (r_y) is the reflectivity of the mirror on the $x-$axis ($y-$axis), and $\delta = L_x - L_y$ is the difference of the armlengths. In even this simple model, we can already see that for identical mirrors and equal arms $E_{\text{ant}} = 0$, giving no signal. Furthermore, if there is a slight perturbation in the relative distance of each arm, we can see $E_{\text{ant}} \neq 0$ and therefore an actual signal will be detected.

We can finally model the deviation of the armlengths through our knowledge of GR. Let us examine the deviation for one arm and suppose the beam splitter and the mirror are test masses in free fall and therefore located according to the geodesic x^μ at the opposite end of the arm, according to the geodesic $x^\mu + \zeta^\mu$, respectively. These geodesic then clearly obeys the geodesic equation:

$$\frac{\mathrm{d}^2 x^\mu}{\mathrm{d}\tau^2} + \Gamma^\mu_{\alpha\beta}(x) \frac{\mathrm{d}x^\alpha}{\mathrm{d}\tau} \frac{\mathrm{d}x^\beta}{\mathrm{d}\tau} = 0, \tag{1.19}$$

$$\frac{\mathrm{d}^2 x^\mu}{\mathrm{d}\tau^2} + \frac{\mathrm{d}^2 \zeta^\mu}{\mathrm{d}\tau^2} + \Gamma^\mu_{\alpha\beta}(x+\zeta) \frac{\mathrm{d}(x+\zeta)^\alpha}{\mathrm{d}\tau} \frac{\mathrm{d}(x+\zeta)^\beta}{\mathrm{d}\tau} = 0. \tag{1.20}$$

Let us now assume the test masses - for our Michelson interferometer these are the beam splitter and mirror - are relatively nearby and slow-moving. (The validity of these assumptions will be discussed later for both types of detector.) This allows us to take the difference of equations (1.5) and (1.20) and expand to the first order in the deviation ζ^μ:

$$\frac{\mathrm{d}^2 \zeta^\mu}{\mathrm{d}\tau^2} + 2\Gamma^\mu_{\alpha\beta}(x) \frac{\mathrm{d}x^\alpha}{\mathrm{d}\tau} \frac{\mathrm{d}\zeta^\beta}{\mathrm{d}\tau} + \zeta^\nu \partial_\nu \Gamma^\mu_{\alpha\beta}(x) \frac{\mathrm{d}x^\alpha}{\mathrm{d}\tau} \frac{\mathrm{d}x^\beta}{\mathrm{d}\tau} = 0. \tag{1.21}$$

From our knowledge of GR, we can also write the equation in the Local Lorentz Frame (LLF). This allows us to use the property that at a point P along the geodesic, the Christoffel symbols $\Gamma^\mu_{\alpha\beta}$ vanish:

$$\Gamma^\mu_{\alpha\beta}(P) = 0. \tag{1.22}$$

Further assuming the slow movement of the test masses, we find that $\mathrm{d}x^i/\mathrm{d}\tau \ll \mathrm{d}x^0/\mathrm{d}\tau$ and therefore reduce equation (1.21) to

$$\frac{\mathrm{d}^2 \zeta^\mu}{\mathrm{d}\tau^2} = -\zeta^\nu \partial_\nu \Gamma^\mu_{00}(x) \left(\frac{\mathrm{d}x^0}{\mathrm{d}\tau} \right)^2. \tag{1.23}$$

We can also simplify the expression by noting the locality of the metric in the LLF

$$g_{\mu\nu} = \eta_{\mu\nu} + \mathcal{O}(x^i x^j), \tag{1.24}$$
$$\partial_0 \Gamma^i_{0\beta} = 0, \tag{1.25}$$

and applying our definition of the Riemann tensor

$$R^i{}_{0j0} = \partial_j \Gamma^i_{00} - \partial_0 \Gamma^i_{0j} = \partial_j \Gamma^i_{00}, \tag{1.26}$$

which results in the final equation:

$$\ddot{\zeta}^i = -c^2 R^i{}_{0j0}\zeta^j = \frac{1}{2}\ddot{h}^{\mathrm{TT}}_{ij}\zeta^j. \tag{1.27}$$

Here we used the property that $R^i{}_{0j0} = R_{i0j0} = -\ddot{h}^{\mathrm{TT}}_{ij}/(2c^2)$, linking the Riemann tensor with the GW in the TT-gauge. Note also that in the LLF $\zeta^0 \approx 0$. A brief view of equation (1.27) tells us this is very Newtonian in nature and we can imagine the effect of a GW on a pair of test masses as that of a small (oscillating) force.

We can now finally examine under which conditions our final equation holds. The two main assumptions we made were that the detector could accurately be described as relatively nearby and therefore in the LLF as well as being slow-moving, meaning much slower than light speed. It must for this reason be noted that these assumptions cannot be made for space-based detectors, but do serve as valid approximations for ground-based detectors.(Li (2024)) As will be discussed later, the response function for all of LISA's detector channels ought to be calculated within the full relativistic geodesic equation, starting from equations (1.5) and (1.20).

Ground-based Detectors

As discussed before, all ground-based GW detectors are more complex versions of physical Michelson interferometers. This section will briefly discuss the current running detectors as well as the next generation of ground-based telescopes such as the Cosmic Explorer and the Einstein Telescope (ET). Furthermore, the latter will be discussed in more detail in particular with regard to its noise modelling.

LIGO-Virgo-KAGRA (LVK)

The first generation of GW detectors to actually directly detect gravitational waves were the two US-based Laser Interferometer Gravitational-Wave Observatories (LIGO) sites, which are located in Hanford, Washington and Livingston, Louisiana, Virgo, located near Pisa, Italy, and the Kamioka Gravitational Wave Detector (KAGRA), located in the Gifu prefecture in Japan. Collectively, they work together under the LIGO-Virgo-KAGRA (LVK) collaboration. Spanning armlengths of 3-4 km, these detectors have been made sensitive for frequencies from approximately human hearing range: between approximately 10 Hz and 10 kHz.(Barish and Weiss (1999)) The first detection was made by the LIGO detectors in 2015, leading to the Nobel prize being awarded to the leading developers of GW in 2017.(Abbott et al. (2016); Nobel Prize committee (2017))

All 4 detectors are simple L-shaped single-detector Michelson interferometers and therefore

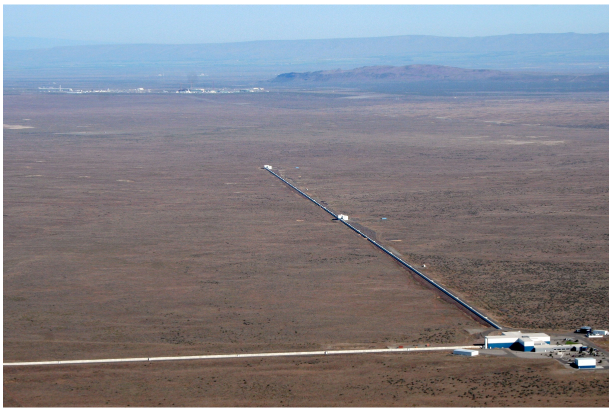

Figure 1.2: Photograph of the LIGO-Hanford, taken from (Wikipedia contributors (2025c)).

work similar to the previous subsection. However, in order to actually detect the gravitational wave, several other measures and technologies ought to be applied on top of the Michelson design.(Li (2024)) Using all these techniques, we arrive at the level of sensitivity possible to detect GWs.

Einstein Telescope (ET) and future ground-based detectors

In order to expand the sensitivity and ranges of frequencies, it's become of interest within the GW community to build new generations of detectors with longer armlengths. Therefore, two notable next generation detectors have been proposed: the Einstein Telescope (ET), which is being strong-armed on the European side, and the Cosmic Explorer, proposed in the United States. Out of these two, the former is in the most advanced stages of development as it has a published blue book, a handful of future building sites for the detector have already been proposed and a final location is expected to be decided in 2026-2027.(ET-EMR collaboration (2025))

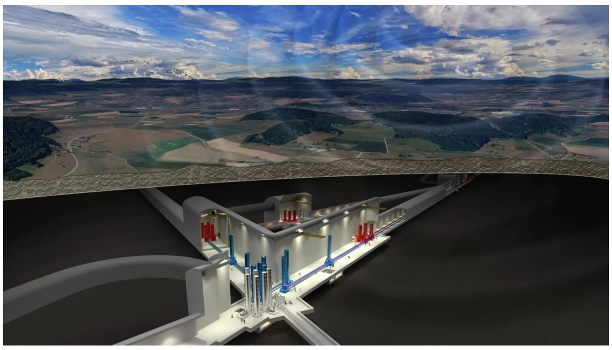

Figure 1.3: Artist illustration of the future ET in the Euregion Meuse Rhine (EMR) region, taken from (ET-EMR collaboration (2025)).

As of February 2025, there are three candidate regions: the Euregion Meuse Rhine (EMR), the island of Sardinia, and the Saxony region, though the last one in a less official capacity.(De Vries (2025)) Furthermore, there are two competing designs for this next detector:

either a network of two L-shaped detectors and a singular triangular design.(ET-EMR collaboration (2025); Abac et al. (2025)) In both designs, the armlengths would be 10-20 kilometers but have clearly distinct orientations. In the latter case, the detectors and lasers would form an equilateral triangle and placed in one site whereas in the former the detectors would be located in two out of three proposed sites.(Wong et al. (2024)) There are several arguments for and against each design. For this thesis project, we would like to emphasise one of the arguments in favour of the triangular design is the exploitation of *correlated noise*.

Recent work has shown that the Parameter Estimation (PE) will perform a lot better when the off-diagonal terms of the noise's covariance matrix is taken into account. It is then further argued that for any network of detectors it is actually beneficial to have correlated noise as they achieve lower uncertainties than if they were located at different places, causing no cross correlations.(Cireddu et al. (2024); Wong et al. (2024))

Space-based Detectors

In spite of the seeming simplicity and seemingly lower amount of confounding variables, space-based detectors are a very different beast from ground-based ones and work in a very different way. While certain Chinese researchers have proposed certain space-based detectors such as TianQin and Taiji, the only officially planned space-based GW detector has been the Laser Interferometry Space Anthenna (LISA), proposed by the European Space Agency (ESA) and National Aeronautics and Space Administration (NASA).(Colpi et al. (2024); Group et al. (2023); Li et al. (2024); Luo et al. (2020)) Planned for launch in 2035, LISA will have a planned operation period from 2037 to 2041.[6]

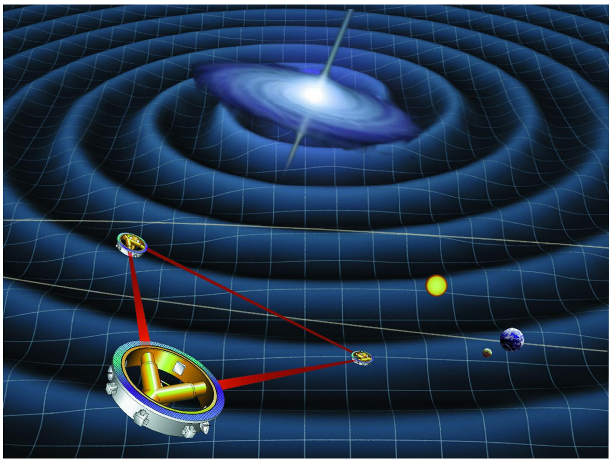

Figure 1.4: Promotional image of LISA, published by NASA, taken from (contributors (2025))

The main advantage and interest for the usage of space-based detectors is their access to much lower frequencies. For example, LISA is expected to measure frequencies between ~ 0.1 mHz and ~ 1 Hz.(Colpi et al. (2024)) With LISA's planned frequency band and sensitivity,

[6]For the uninitiated reader, this does not necessarily mean LISA will cease operation after 4 years, but the mission will only have a guaranteed two year lifespan. After the planned period of operation, it will be examined whether the mission can be continued.

an entirely new range of signals are expected to be detected of a totally different kind. In fact, this collection of potential signals comes both astrophysical and cosmological sources that all have interesting science goals associated with them. Various expected sources include the following(Colpi et al. (2024)):

- **Galactic Binary (GB)**: as the name implies, these are binary systems of compact objects (e.g. a Black Hole (BH), Neutron Star (NS), or in most cases, a White Dwarf (WD)) which are slowly orbiting each other. Given their slow orbital decay, they produce quasi-monochromatic GWs across their detection period. Their study has much astrophysical importance, more specifically with respect to their structure and evolution, serving as one of the major multimessenger source candidates. It is also expected their multimessenger potential will allow us to answer problems in cosmology such as the Hubble tension. For example, they would fill a similar role to standard candles in cosmology and thus serve as an independent measure for the Hubble constant, hence their status as *standard sirens*.

- **Extreme-Mass Ratio Inspiral (EMRI)**: these are systems where the mass ratio is below $\sim 10^{-4}$, usually one stellar-mass compact object orbiting a Supermassive Black Hole (SMBH). Aside from the same cosmological uses they serve alongside GBs, one of the major motivations for the study of EMRIs are their use as a test for GR. As the compact objet spirals into SMBH, the spacetime curvature becomes much stronger, causing the compact object to etch out the metric, thus allowing us to analyse our assumptions in GR as well as to prod so-called *beyond-vaccuum GR* effects. These effects could range from astrophysical origins such as an accretion disk or even indicate new physics beyond classical General Relativity.(Katz et al. (2021); Group et al. (2023))

- **Stochastic Gravitational Wave Background (SGWB)**: Since various astrophysical sources peak in the same frequency band and are expected to number on the order of thousands, they will become so hard to discern they will form closer to a background noise than resolvable signals. On top of those sources, it's thought so-called *primordial gravitational waves* - GWs created in the early universe due to phase transitions similar to the Cosmic Microwave Background (CMB) found in the EM spectrum - would become detectable as well. This would have implications for finding out the origins of the universe.

However, this comes with its own set of unique challenges. To start, it is not possible to perform actual physical interferometry in space due to the large distance making the laser's intensity too weak when it arrives at each arm's end and the orbit will almost always guarantee the armlengths will vary with time. This makes the data analysis for all space-based detectors very different.(Bayle and Hartwig (2023); Hartwig and Muratore (2022))

For one, instead of 3 data streams, LISA is a constellation of 3 spacecraft that together produce 6 data streams created by 6 single link laser phase measurements.(Colpi et al. (2024)) As will be discussed in the methodology, the laser frequency noise caused by the single links are orders of magnitude too high to be able to detect any signals on their own. Therefore a technique named Time-Delay Interferometry (TDI) has been proposed for analysing LISA data.(Tinto and Dhurandhar (2021)) Essentially what TDI does, is performing Michelson interferometry, or simulating other types of interferometers such as a Sagnac interferometer, in the data processing stage instead of building a physical one as is done for ground-based detectors. This happens through the stacking of delayed signals on top of each other in such a way that the laser noise is cancelled out.

Another great challenge for LISA analysis in particular is the so-called *Global Fit*.(Katz et al. (2024); Colpi et al. (2024)) Due to the fact LISA is expected to be so sensitive for many different sources, this apparent blessing becomes more of a curse as there are currently no known techniques to detect and estimate all these signals which will oftentimes be overlapping. For certain sources, they will be so omnipresent and consistent they will act more like background noise than an individual signal, similar to the ambiance in a busy bar or concert hall. Nevertheless, it is of astrophysical interest to be able to differentiate these various background signals and many other foreground signals are expected to overlap as well.

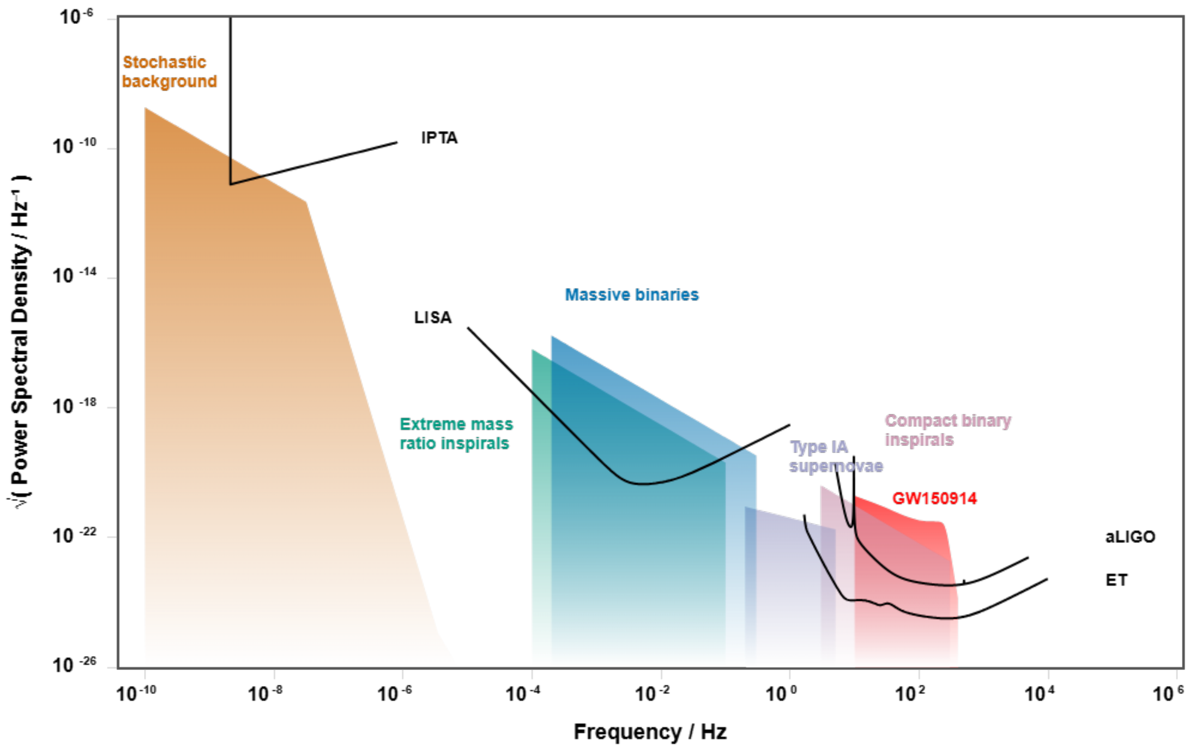

Figure 1.5: Graph demonstrating the PSD curves and corresponding relevant sources for PTAs (e.g. IPTA), LISA and the groud-based detectors ET and (advanced) LIGO (aLIGO). Taken from (Moore et al. (2014))

Comparing ET and LISA

The most important difference between ET and LISA, at least for this project, is their noise curves and their response generation. Figure 1.5 shows their respective (estimated) strain across various expected GW sources. An important difference in their matrices is the fact the current LISA noise models imply 0 noise at certain frequencies due to consequences from TDI. The effects of the numerical errors and methods to mitigate them will be discussed in the next chapter. Furthermore, ET, like with all ground-based detectors, has a linear relationship between the GW waveform and the detector strain through the long wavelength approximation ($L_{\text{detector}} \ll \lambda_{\text{GW}}/2\pi$).(Li (2024)) Through the same linearity, one can also implement waveform models which are immediately in the frequency-domain. This lack of linearity makes the response generation for LISA much less trivial and more computationally expensive as will be discussed in more detail in the methodology. Finally, one can find a summary of the relevant differences and similarities in Table 1.1. With respect to the scientific

Detector	Einstein Telescope	LISA
Effective frequency range [Hz]	$[10^0, 5 \times 10^3]$	$[10^{-4}, 10^0]$
Detector shape	Triangular (or 2 L-shapes)	Triangular
Type of interferometer	3 connected Michelson interferometers (or 2 separate detectors)	6 single-link detectors, can be formed into Michelson, AET or Sagnac variables
Uncorrelated noise sources	Thermal noise, quantum noise, shot noise	laser frequency noise, OMS noise, TM noise, other second order noises...
Correlated noise sources	seismic noise, Newtonian noise	correlation caused by TDI
Expected GW sources	CBCs, SNe, SGWB, etc.	EMRIs, GBs, MBHBs, SGWB, etc.
Location	Limburg, Sardinia, and/or Saxony (approx. stationary for most signals)	ESA orbit at around 1 AU
Planned launch date	decision location(s) in 2026-2027, start construction afterwards	2035
Expected period of operation	2035-2085	2037-2042 (minimum mission duration of 4.5 years)

Table 1.1: Summary of the relevant differences between the Einstein Telescope and LISA. Based on (Colpi et al. (2024)) and (Abac et al. (2025)).

interaction between both detectors, is also some potential for the cooperation between ET and LISA, namely in multiband sources. To start, a few of the potential mutual benefits could be early warning of certain merger events as a heavy GB detected by LISA can become a detectable Compact Binary Collisions (CBC) for ET and LVK.(Abac et al. (2025))

1.3 GW Data Analysis

In order to probe a GW signal, more advanced data analysis techniques ought to be used than simple linear fits. More exactly, Bayesian statistics are employed, from which we find a probability distribution for the fit parameters and therefore determine the most likely values.

Detector noise

For GW detectors and signal processing in general, noise becomes an utterly significant part of the analysis. For this, the Signal-to-Noise Ratio (SNR) serves as a metric for the 'loudness' of a signal compared to the signal noise. For a single GW detector, this is calculated with the following inner product:

$$(a|b) = 4\mathrm{Re}\left[\int_0^\infty \frac{\tilde{a}(f)\tilde{b}^\dagger(f)}{S(f)}\mathrm{d}f\right] \tag{1.28}$$

where $\tilde{a}$ is the Fourier transform of a signal a and $S(f)$ is the so-called Power Spectral Density (PSD) of the detector.(Li (2024); Maggiore (2017)) This can physically be interpreted as the variance on the amplitude of the random noise at a certain frequency, on the assumption the noise is approximately Gaussian. More exactly, we can define the PSD by relating it to the averaged square magnitude of the noise n at frequency f:(Hartwig et al. (2023))

$$< \tilde{n}^\dagger(f)\tilde{n}(f') >= \delta(f-f')\frac{1}{2}S(f). \tag{1.29}$$

For networks of detectors, this inner product can be expanded to the following form:(Cireddu et al. (2024))

$$\begin{aligned}(\mathbf{a}|\mathbf{b}) &= 4\mathrm{Re}\left[\int_0^\infty \tilde{\mathbf{a}}\cdot(\mathbf{S}^{-1})\cdot\tilde{\mathbf{b}}^\dagger \mathrm{d}f\right], &(1.30)\\ &= 4\sum_{K,M}\mathrm{Re}\left[\int_0^\infty \tilde{a}_K(f)(S^{-1})_{KM}\tilde{b}_M^\dagger(f)\mathrm{d}f\right]. &(1.31)\end{aligned}$$

In this case, we no longer speak of one signal but an array of signals $\tilde{\mathbf{a}}$ with a covariance matrix $\mathbf{S}(f)$ with a PSD in the diagonal and a Cross Power Spectral Density (CSD) in the off diagonals, which can analogously be defined through the averaged noise covariance between two detectors K and M:(Cireddu et al. (2024))

$$< \tilde{n}_K^\dagger(f)\tilde{n}_M(f') >= \delta(f-f')\frac{1}{2}S_{KM}(f). \tag{1.32}$$

We can then finally define the SNR as

$$\mathrm{SNR}[h] = \sqrt{(h|h)}. \tag{1.33}$$

Bayesian Statistics

Bayesian statistics fully arises from Bayes' theorem:

$$P(A|B) = \frac{P(B|A)P(A)}{P(B)}, \tag{1.34}$$

which describes the probability of A given B can be determined through the probabilities of B, and A and the conditional probability B happening given A.(Ross (2019)) When applying this to data analysis, one usually speaks of trying the find the posterior distribution of a set of parameters θ for given measurement data d, which turns the previous equation into the following expression:

$$P(\theta|d) = \frac{P(d|\theta)\pi(\theta)}{P(d)} = \frac{P(d|\theta)\pi(\theta)}{\int P(d|\theta)\pi(\theta)\mathrm{d}\theta}. \tag{1.35}$$

Here, $P(\theta|d)$, $P(d|\theta)$, $\pi(\theta)$ and $P(d)$ are named the posterior, likelihood, prior and evidence, respectively. One can physically interpret each variable the following ways.(Ross (2019); Li (2024))

- Posterior $P(\theta|d)$: the refined probability distribution of your physical parameters with the extra information of the data.
- Prior $\pi(\theta)$: all prior knowledge and assumptions of the possible physical parameters before taking the data into account.
- Likelihood $P(d|\theta)$: also written as $\mathcal{L}(\theta)$, it can be seen as the probability a certain model would produce this data. For example, in case of a signal it would determine whether the residual data without the signal is just pure noise.
- Evidence $P(d)$: there is less of a useful physical interpretation for this value except for a normalising weight by integrating or summing over the total parameter space $P(d) = \int P(d|\theta)\pi(\theta)\mathrm{d}\theta$. Though irrelevant in most cases, it is important when comparing the validity between models, e.g. whether a CBC signal comes from a NS or BH binary.

In the field of GW data analysis, the likelihood holds a high level of importance in its calculation process and will as a consequence. As stated before, the detector's noise characterisation fully determines the likelihood. More exactly, for a signal $s(\theta)$ and data $d = s(\theta)+n$, the likelihood is found to be $P(d|\theta) = P(d-s(\theta) = \hat{n})$. For most detector noise sources, it is assumed they are Gaussian in nature.(Legin et al. (2023); Buscicchio et al. (2024)) The log of the likelihood then becomes proportional to the inner product of the residual noise. For example, in case of LISA's Michelson variables, this becomes

$$\begin{aligned}\log(P(d|\theta)) &= -\frac{1}{2}(d-s(\theta)|d-s(\theta)), \\ &= -\frac{1}{2}\sum_{K,M\in\{X,Y,Z\}} \mathrm{Re}\left[\int (d_K - s_K(\theta))^\dagger (S^{-1})_{KM}(d_M - s_M(\theta))\mathrm{d}f\right]\end{aligned} \tag{1.36}$$

with d_K and $s_K(\theta)$ the data and waveform for Michelson variable $K \in \{X, Y, Z\}$.

In the field of GW data analysis, it is often very hard to calculate $\pi(\theta)$ and normalise the posterior. For this reason, approximations and other numerical approaches are made to nevertheless quantify the uncertainties. The easiest approximation one can make is to assume the posterior distribution is a multivariate normal distribution around the true parameter values. One can then find the (inverse of the) corresponding covariance matrix through the Fisher Information Matrix (FIM) defined as the expected value of the second derivatives for the log-likelihood:(Li (2024); Gair et al. (2022))

$$\mathcal{F}_{ij} = -\mathrm{E}\left[\left.\frac{\partial^2 \log(P(d|\theta))}{\partial\theta_i\partial\theta_j}\right|\theta\right]_{\theta=\theta_{\mathrm{true}}}, \tag{1.37a}$$

$$= \frac{1}{2}\mathrm{E}\left[\left.\frac{\partial^2}{\partial\theta_i\partial\theta_j}(d-s(\theta)|d-s(\theta))\right|\theta\right]_{\theta=\theta_{\mathrm{true}}}. \tag{1.37b}$$

Here, θ_i is the $i-$th fit parameter. A simple derivation will in turn show this is equivalent to the following expression:

$$\mathcal{F}_{ij} = (\partial_i s(\theta)|\partial_j s(\theta))_{\theta=\theta_{\mathrm{true}}}, \tag{1.38}$$

with $\partial_i = \partial/\partial\theta_i$. We can then relate the FIM to the covariance matrix the following manner. If one assumes the posterior distribution $\theta|d$ follows a multivariate gaussian distribution around the true parameters μ_θ with a covariance matrix of Σ_θ, i.e.

$$\theta|d \sim \mathcal{N}(\mu_\theta, \Sigma_\theta). \tag{1.39}$$

Then through equation (1.37), we see that[7]

$$\mathcal{F}_{ij} = (\Sigma_\theta)^{-1}_{ij}. \tag{1.40}$$

The drawback to this approximation is that it holds no value when trying to infer parameters from real data and only serves as an estimate for the uncertainties. Furthermore, the Gaussian approximation is often not valid as multimodal posteriors are not uncommon, for example. In any case, the comparatively low computational cost often makes it nonetheless a useful first step in gauging the uncertainties.

The most proper numerical method to estimate the posterior distribution can be found in the class of Markov Chain Monte Carlo (MCMC) algorithms. These are a collection of probabilistic algorithms in order to sample a distribution which converges to the desired posterior without knowing its normalised form. Each MCMC sampling algorithm has the same basic structure, based on the Hastings-Metropolis algrotithm.(Ross (2019)) Suppose first that $P(\theta|d) \propto g(\theta)$, where g is a known function. One then follows the following steps:

0. Randomly sample a point θ_0 from the prior distibrution.

1. For each sampled point θ_n, one 'chooses[8] a candidate new point y_n around θ_n.'

2. Calculate $\alpha = \min\{1, g(y_n)/g(\theta_n)\}$.

3. Randomly sample u, which is uniformly distributed between 0 and 1: $u \sim U[0, 1]$.

4. If $u < \alpha$, then $\theta_{n+1} = y_n$, otherwise $\theta_{n+1} = \theta_n$.

5. Repeat steps 1 to 4.

The end result should then converge to the true posterior distribution. While being the most mathematically valid option to find $P(\theta|d)$, there are a lot of computational costs associated with most MCMC algorithms, particularly in the calculation of the likelihood as the waveform and response signal $s(\theta_n)$ are often non-trivial computations.(Wong et al. (2023); Wouters et al. (2024)) It is therefore become of high interest to develop algorithms which optimise for and speed up the convergence time.

[7]Implicitly, we also assume that the prior distribution are flat or uniform, i.e. $\theta_i \sim \mathcal{U}[a_i, b_i]$.

[8]The method by which a candidate point is chosen, is where each MCMC algorithm usually differs. For the simplest types, one samples y_n as a random variable following normal distribution centered at θ_n with a predetermined covariance matrix Σ_θ, i.e.: $y_n \sim \mathcal{N}(\theta_n, \Sigma_\theta)$. For example, another method used by Hamiltonian MCMCs is to solve some form of the Hamiltonian equations for N steps with initial condition $x_n(0) = \theta_n$ and to let y_n be the final point: $y_n = x(N\Delta t)$.(Wikipedia contributors (2025b))

1.4 Motivation

Inspired by work conducted by (Katz et al. (2022)) and (Cireddu et al. (2024)), this thesis will attempt to assess the impacts of different noise models to the data analysis of LISA foreground signals. More exactly, the cases between a symmetric noise model (i.e. when all single-link noise parameters and orbit parameters are symmetric: $A_{ij} = A$, $P_{ij} = P$, $L_{ij}(t) = L$) and the more general asymmetric model. It has already been shown approximating LISA's true orbit for one with equal armlengths causes biases in the posterior distribution. As it is therefore expected these asymmetries may cause biases or cause us to overestimate the accuracy in our analysis, this work attempts to assess the data analysis effects caused by the asymmetric noise.

Chapter 2

Methodology

There are known knowns; there are things we know we know. We also know there are known unknowns; that is to say we know there are some things we do not know. But there are also unknown unknowns – the ones we don't know we don't know.
- Donald Rumsfeld, US secretary of Defense during the Bush administration (2002)

2.1 GW source model

Before performing a proper analysis, a signal needs to be injected for some kind of event and therefore a source needs to be chosen. For this thesis project, this was decided to be galactic binaries. Being one of the simplest potential sources, these have the following fully analytic waveform - i.e. the $+$- and $\times$-polarisations' equations - in the source frame:(Katz et al. (2022))

$$h_+(t|A, f_0, \dot{f}_0, \phi) = A\cos\left(2\pi\left[f_0 t + \frac{1}{2}\dot{f}_0 t^2 + \frac{1}{6}\ddot{f}_0 t^3\right] + \phi_0\right), \tag{2.1a}$$

$$h_\times(t|A, f_0, \dot{f}_0, \phi) = A\sin\left(2\pi\left[f_0 t + \frac{1}{2}\dot{f}_0 t^2 + \frac{1}{6}\ddot{f}_0 t^3\right] + \phi_0\right). \tag{2.1b}$$

Here, the amplitude A, initial frequency f_0, initial frequency rate of change $\dot{f}_0$, and initial phase ϕ_0 are input parameters. Furthermore, the second derivative $\ddot{f}_0$ is defined as $\ddot{f}_0 = 11\dot{f}_0^2/3f_0$ after using the identity

$$\dot{f}(t) = \frac{96}{5}\pi^{\frac{8}{3}}\left(\frac{\mathcal{M}_c G}{c^3}\right)^{\frac{5}{3}} f^{\frac{11}{3}} \propto f^{\frac{11}{3}}, \tag{2.2}$$

where we $\mathcal{M}_c$, G, and c are the chirp mass, Newtonian gravitational constant and the speed of light, respectively.(Katz et al. (2022)) These Finally we assume the higher order terms past the second order become negligible. We also note the identity writing A in terms of the same physical parameters along with the distance to the binary d_L:[1]

$$A(\mathcal{M}_c, f_0, d_L) = 2\frac{(G\mathcal{M}_c)^{\frac{5}{3}}}{c^4 d_L}(\pi f)^{\frac{2}{3}}. \tag{2.3}$$

[1] It is also with these parameters that we are able to find an independent measure for the cosmic distance ladder and thus are able to calculate the Hubble constant H_0.(Schutz (1986))

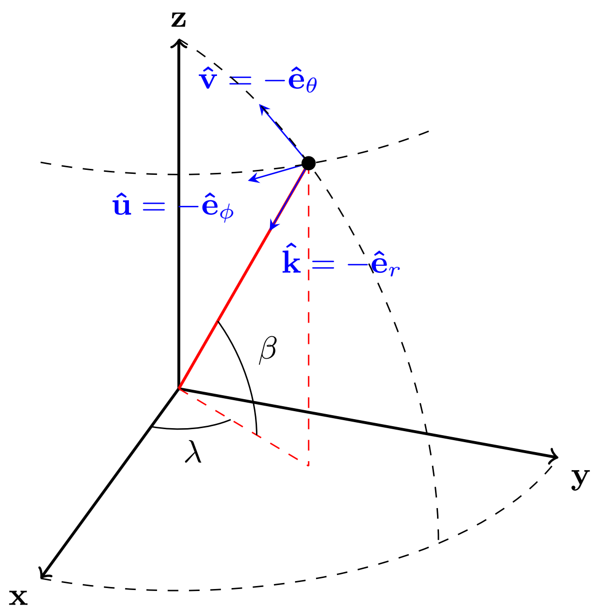

Figure 2.1: Diagram demonstrating the $(\hat{u}, \hat{v}, \hat{k})$ basis in the SSB coordinates, taken from (Katz et al. (2022)).

However, these polarisation elements still need to be written in function of the Solar system's barycentric (SSB) basis. Looking at figure 2.1 and applying our knowledge of trigonometry, we can write the wave propagation basis $(\hat{u}, \hat{v}, \hat{k})$ - with $\hat{k}$ the direction of propagation and - in terms of the SSB basis, or more specifically the ecliptic latitude β and longitude λ:

$$\hat{k} = -(\cos\beta\cos\lambda, \cos\beta\sin\lambda, \sin\beta), \tag{2.4a}$$

$$\hat{v} = -(\sin\beta\cos\lambda, \sin\beta\sin\lambda, -\cos\beta), \tag{2.4b}$$

$$\hat{u} = (\sin\lambda, -\cos\lambda, 0). \tag{2.4c}$$

Finally, the transformation for the GW polarisations from the source frame to the SSB frame is calculated through the following relation, using the inclination and polarisation angles ι and ψ:(Katz et al. (2022))

$$\begin{pmatrix} h_+^{\mathrm{SSB}} \\ h_\times^{\mathrm{SSB}} \end{pmatrix} = -\begin{pmatrix} \cos 2\psi & -\sin 2\psi \\ \sin 2\psi & \cos 2\psi \end{pmatrix} \begin{pmatrix} (1+\cos^2(\iota))h_+ \\ 2\cos(\iota)h_\times \end{pmatrix}. \tag{2.5}$$

2.2 Response function for space-based GW detectors

As mentioned before, the response function cannot easily be determined in the frequency domain as opposed to the case in ground-based detectors. Due to the vastly longer armlengths of LISA, the assumption made in the step made implicitly in (1.7), namely particularly in the fact that the arms are short enough such that the light path experiences the same metric pertubation across the light's geodesic. This assumption is only valid for when the armlength is much shorter than the reduced wavelength of the GW $\lambda_{\mathrm{GW}}/2\pi$:

$$L \ll \frac{\lambda_{\mathrm{GW}}}{2\pi}. \tag{2.6}$$

For LVK ($\lambda_{\mathrm{GW}}/2\pi \sim 10^5$m, $L \sim 10^3$m), this assumption is valid, but it will not be valid for LISA ($\lambda_{\mathrm{GW}}/2\pi \sim 10^{10}$m, $L \sim 10^9$m).(Li (2024)) Therefore, a new approach must be made in order to estimate the strain responses for a single link. Let us start by defining our general deformation in (1.12). For a single link in a space-detector, the antenna patterns for a single link are defined as:(Katz et al. (2022))

$$F_{+,ij} = (\hat{u} \cdot \hat{n}_{ij})^2 - (\hat{v} \cdot \hat{n}_{ij})^2, \tag{2.7a}$$

$$F_{\times,ij} = 2(\hat{u} \cdot \hat{n}_{ij})(\hat{v} \cdot \hat{n}_{ij}). \tag{2.7b}$$

The deformation for a single link $H_{ij}(t)$ along a null-geodesic $(\vec{x}(\lambda), t(\lambda))$ then becomes

$$H_{ij}(\vec{x}(\lambda), t(\lambda)) = F_{ij,+} h_+^{\mathrm{SSB}}(t(\lambda)) + F_{ij,\times} h_\times^{\mathrm{SSB}}(t(\lambda)). \tag{2.8}$$

For both equations, the normed vector $\hat{n}_{ij}(t)$ is named the *link unit vector* to receiver i from emitter j, defined as $\vec{x}_i - \vec{x}_j \equiv ||\vec{x}_i - \vec{x}_j||\hat{n}_{ij} = L_{ij}\hat{n}_{ij}$. Furthermore, $h_{+,\times}^{\mathrm{SSB}}$ are the polarisation terms in the SSB frame. For our space-based detectors, we further make the approximation the geodesic light path is a linear straight line, giving us the following parameter equations:

$$\vec{x}(\lambda) \approx \vec{x}_j + \lambda \hat{n}_{ij}, \tag{2.9a}$$

$$t(\lambda) \approx t_j + \frac{\lambda}{c}. \tag{2.9b}$$

Note also then that $\vec{x}(L_{ij}) = \vec{x}_j$ and $t(L_{ij}) = t_j$. This approximation allows us to write H_{ij} as a simple function with one dependency:

$$H_{ij}(\vec{x}(\lambda), t(\lambda)) = H_{ij}\left(t(\lambda) - \frac{\hat{k} \cdot \vec{x}(\lambda)}{c}\right), \tag{2.10a}$$

$$= H_{ij}\left(t_j - \frac{\hat{k} \cdot \vec{x}_j}{c} + \frac{1 - \hat{k} \cdot \hat{n}_{ij}}{c}\lambda\right). \tag{2.10b}$$

After integration, the strain of a single link y_{ij} at the arrival time t_j becomes

$$y_{ij}(t_j) = \frac{1}{2(1 - \hat{k} \cdot \hat{n}_{ij}(t_j))}\left[H_{ij}\left(t_j - \frac{\hat{k} \cdot \vec{x}_j(t_j)}{c}\right) - H_{ij}\left(t_j - \frac{\hat{k} \cdot \vec{x}_j(t_i)}{c} + \frac{1 - \hat{k} \cdot \hat{n}_{ij}(t_i)}{c} L_{ij}(t_i)\right)\right]. \tag{2.11}$$

One final approximation is now finally made by assuming the spacecraft is slow-moving compared to the light travel path time, i.e. $\vec{x}_i(t_i) \approx \vec{x}_i(t_j)$ and therefore also $L_{ij}(t_i) \approx L_{ij}(t_j)$ and $\hat{n}_{ij}(t_i) \approx \hat{n}_{ij}(t_j)$. We can then finally write our single link strains solely as a function of reception time t_i:

$$y_{ij}(t_i) = \frac{1}{2(1 - \hat{k} \cdot \hat{n}_{ij}(t_i))}\left[H_{ij}\left(t_i - \frac{\hat{k} \cdot \vec{x}_j(t_i)}{c} - \frac{L_{ij}(t_i)}{c}\right) - H_{ij}\left(t_i - \frac{\hat{k} \cdot \vec{x}_i(t_i)}{c}\right)\right]. \tag{2.12}$$

Due to the various numerical challenges in calculating these functions, a set of numerical code packages have been developed. The Python package `fastlisaresponse` was orignally chosen to turn the waveforms into a time domain response.(Katz et al. (2022)) This open source package allows one to compute the signal responses and compute the corresponding TDI delays for any provided orbit of 3 spacecraft. Finally, the time-domain signal responses will then be represented in the frequency domain via a Fast Fourier Transform (FFT).

2.3 Time-Delay Interferometry (TDI)

In spite of the, single-link responses do not suffice by themselves to extract the GWs due to the laser noise, which is estimated to be up to 8 orders of magnitude larger than any other noise sources or expected GW signals. For this reason, it has become of high interest to the LISA community to devise data processing techniques in order to suppress this noise source. The current most popular solution to this problem has been Time-Delay Interferometry (TDI).(Tinto and Dhurandhar (2021); Bayle (2019))

TDI can intuitively be understood as the summing of delayed single-link data in order to simulate interferometers that do normally suppress laser frequency noise in their physical interferometry. The processed data then becomes the so-called *TDI variables* which are dependent on the type of interferometer used. In the literature, the variables made from simulating a triangular Michelson interferometer are noted as (XYZ) whereas the variables simulating a Sagnac interferometer are written as $(\alpha\beta\gamma\zeta)$ (e.g. Tinto and Dhurandhar (2021); Hartwig et al. (2023); Alvey et al. (2024)). As will be demonstrated in the appendix, the corresponding covariance matrices for nearly. However, under certain approximations, one can deduce that the (cross-)power spectral density becomes symmetric, i.e.:[2]

$$< \tilde{n}_K^\dagger(f)\tilde{n}_L(f) >=< \tilde{n}_M^\dagger(f)\tilde{n}_N(f) >, \tag{2.13}$$

and

$$< |\tilde{n}_K(f)|^2 >=< |\tilde{n}_N(f)|^2 > . \tag{2.14}$$

for TDI variables $K \neq L$ and $N \neq M$. This simplification allows us to diagonalise the covariance matrix through the so-called (quasi-)orthogonal (AET) base, named after its inventors Armstrong (A), Estabrook (E), and Tinto (T).(Bayle (2019)) A more detailed derivation of these variables can be found the appendix A as well.

Let us now illustrate how TDI successfully suppresses the laser frequency noise. We first define the delay operator $\mathcal{D}_{ij}(t)$, which delays a function according to the (time-dependent) armlength L_{ij} from emitting spacecraft i to receiving spacecraft j, as illustrated in figure 2.2:

$$\mathcal{D}_{ij}[y](t) = y(t - L_{ij}(t)). \tag{2.15}$$

Suppose we want to emulate one Michelson interferometer through stacking single-link phases, we will have 4 phase measurements for each arm. Examining the first arm going between detector 1 and 2, we can physically intuit using (1.17) and (1.18) that the terms represent the phase measurement of the first ongoing beam, the final phase measurement of a returning beam $\mathcal{D}_{12}y_{21}(t)$, and their counterparts after being reflected to and from the detector 3, respectively $-\mathcal{D}_{13}\mathcal{D}_{31}y_{12}(t)$ and $-\mathcal{D}_{13}\mathcal{D}_{31}\mathcal{D}_{12}y_{21}(t)$. All together, we can then write the entire Michelson variable X as the following sum of delayed single-link beams:(Tinto and Dhurandhar (2021))

$$X = (1 - \mathcal{D}_{13}\mathcal{D}_{31})[y_{12} + \mathcal{D}_{12}[y_{21}]] - (1 - \mathcal{D}_{12}\mathcal{D}_{21})[y_{13} + \mathcal{D}_{13}[y_{31}]]. \tag{2.16}$$

[2] Another interesting consequence of this is that the CSD must also be fully real. This can be shown through the short proof:
$< \tilde{n}_K^\dagger(f)\tilde{n}_L(f) >= (< \tilde{n}_K(f)\tilde{n}_L^\dagger(f) >)^\dagger = (< \tilde{n}_L(f)\tilde{n}_K^\dagger(f) >)^\dagger \implies < \tilde{n}_K^\dagger(f)\tilde{n}_L(f) > \in \mathbb{R}$.

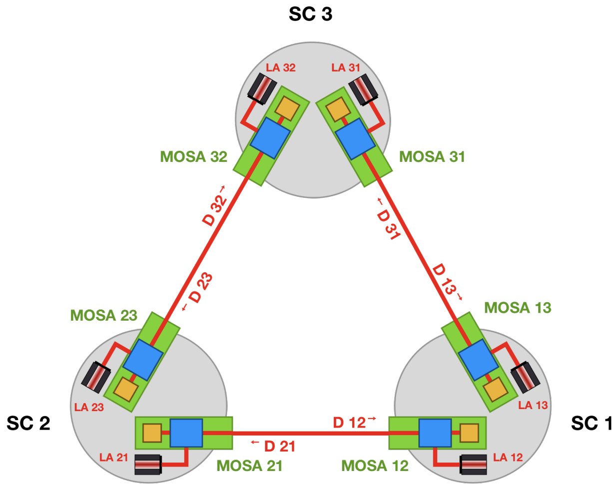

Figure 2.2: A diagram showing the setup and illustrating the convention notation for TDI, taken from (Katz et al. (2022))

Basing on derivations shown by (Bayle (2019); Tinto and Dhurandhar (2021)), we can demonstrate the claimed suppression. Supposing we have a common phase noise $C(t)$ at each arm return next to a signal s_{ij}, i.e.

$$y_{ij}(t) + \mathcal{D}_{ij}[y_{ji}](t) = (1 - \mathcal{D}_{ji}\mathcal{D}_{ij})C(t) + s_{ij}(t), \tag{2.17}$$

one can then determine that the first term becomes:

$$(1 - \mathcal{D}_{13}\mathcal{D}_{31})[y_{12} + \mathcal{D}_{12}[y_{21}]](t) = (1 - \mathcal{D}_{13}\mathcal{D}_{31})(1 - \mathcal{D}_{21}\mathcal{D}_{12})C(t) + s_{12}(t) - \mathcal{D}_{13}\mathcal{D}_{31}s_{12}(t), \tag{2.18}$$

and similarly, the second term becomes:

$$(1 - \mathcal{D}_{12}\mathcal{D}_{21})[y_{13} + \mathcal{D}_{13}[y_{31}]](t) = (1 - \mathcal{D}_{12}\mathcal{D}_{21})(1 - \mathcal{D}_{13}\mathcal{D}_{31})C(t) + s_{13}(t) - \mathcal{D}_{12}\mathcal{D}_{21}s_{13}(t). \tag{2.19}$$

Taking the difference between both terms, we finally find that the common phase term vanishes if and only if the operators $\mathcal{D}_{13}\mathcal{D}_{31}$ and $\mathcal{D}_{12}\mathcal{D}_{21}$ commute: $[\mathcal{D}_{13}\mathcal{D}_{31}, \mathcal{D}_{12}\mathcal{D}_{21}] = 0$.

While not valid under general conditions, this identity is in fact true for the case where the armlength L_{ij} are constant across time! This simple construction is the derivation for the first generation Michelson variable and correctly suppresses all laser frequency noise. However, the general case will have that $[\mathcal{D}_{13}\mathcal{D}_{31}, \mathcal{D}_{12}\mathcal{D}_{21}] \neq 0$ and therefore various other improvements to this technique ought to be made.

In order to improve on the accuracy of the response functions and noise modelling, one can also use higher generations which factor in the armlengths' time dependence. These refinements would then ensure a suppression of the laser frequency noise to a sufficient degree such that it can be ignored in analysis, or more exactly such that the remaining laser frequency noise falls below secondary noise levels. Since there is no single way of suppressing the remaining laser frequency noise, various higher generation suggestions exist for the used TDI-1 variables, which are provided in the appendix A below.

One of the major issues with TDI is the so called *TDI artifacts*. As will be shown on the appendix A, a problematic consequence brought about by the assumption of constant arm-lengths is that the corresponding covariance matrix will have a factor $\cos(4\pi f L)$. This would imply there would be 0 noise at frequencies $f \in \{k/2L | k \in \mathbb{N}\}$, which both does not correspond to physical phenomena and more importantly causes various numerical issues.

While a corresponding signal would at these TDI zero-points normally be cancelled out alongside the remaining noise, there still rests an effective residual signal because of the artifacts brought about by the necessary numerical calculations.

2.4 Data analysis

The comparison between the various noise models and TDI channels will happen in 3 parts. Firstly, the noise-free SNR will be calculated to address the numerical instabilities that may arise as will be discussed in more detail. Secondly, the FIM will be calculated for a few noise model cases. Finally, a full Bayesian analysis will be attempted through a modified version of `JIM`, a JAX-based GW inference toolkit.(Wong et al. (2023); Wouters et al. (2024)) For all parts of the analysis, the covariance matrix will be produced with constant and equal arms. The symmetric and asymmetric noise models refer to the cases when the single-link TM and OMS noise parameters - A_{ij} and P_{ij}, resp. - are either equal or unequal. More specifically the symmetric noise model will set $A_{ij} = 3$ and $P_{ij} = 15$, whereas the asymmetric noise model $A_{ij} = \{3.61, 3.02, 2.87, 3.43, 2.65, 3.45\}$ and $P_{ij} = \{14.00, 16.93, 9.43, 21.55, 17.04, 20.83\}$ for all $ij \in \{12, 23, 31, 21, 32, 13\}$. These values have been chosen such that the average of the parameters correspond to the symmetric noise model, in line with (Hartwig et al. (2023)).

Comparing and calculating the SNRs

As stated before and can be seen in the derivations for the covariance matrix in appendix A, the assumption of equal and constant arms produces a covariance proportional to $\sin(2\pi f L)$. This would imply the covariance matrix goes to zero and becomes singular at around the points $f_k = k/2L$. One can then expect the numerical errors from inverting this matrix for frequencies around these *TDI modes*. This part of the thesis will then address the potential effects of the TDI artifacts and introduce methods to mitigate them. For this project, two methods in resolving the TDI artifacts are proposed: masking the TDI modes, and regularisation.

The first method that will be discussed is masking. Here, the inner product is not calculated over frequencies around a 1% bar between each mode. More specifically, $(\mathbf{a}|\mathbf{b})$ becomes:

$$(\mathbf{a}|\mathbf{b}) = \int_0^\infty \tilde{\mathbf{a}} \cdot (\mathbf{S}^{-1}) \cdot \mathbf{b}^\dagger \chi(f) \mathrm{d}f, \tag{2.20}$$

where $\chi(f)$ is defined as:

$$\chi(f) = \begin{cases} 0 & f \in \bigcup_{n\in\mathbb{N}} \left[\frac{n-0.01}{2L}, \frac{n+0.01}{2L}\right], \\ 1 & \text{else.} \end{cases} \tag{2.21}$$

The choice of 1% was made as it seemed a reasonable estimate without disregarding too much of the frequency range. This would then avoid the peaks where the matrix becomes ill-conditioned. Figure 2.3 shows the condition number, which indicates the expected numerical

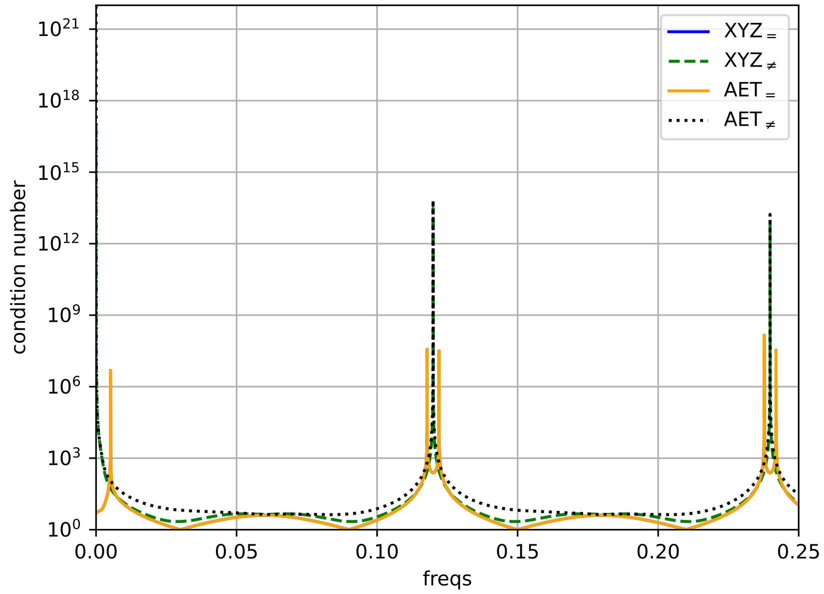

Figure 2.3: Figure showing the condition number for the covariance matrix in all cases

instability, for each relevant channel for both noise models.

Furthermore, the manner by which regularisation suppresses the artifacts, is by adding an extra term for the PSDs for each TDI channel. This method can also be physically justified as including the second order noise sources, with the residual single-link laser noise in particular.(Hartwig and Muratore (2022)) The regularised PSDs $S^{XX}_{(\mathrm{reg})}$, $S^{YY}_{(\mathrm{reg})}$, and $S^{ZZ}_{(\mathrm{reg})}$ are then defined as

$$S^{XX}_{(\mathrm{reg})} = S^{XX}_{(\mathrm{none})} + 10^{-42}\ \mathrm{Hz}^{-1}, \tag{2.22a}$$
$$S^{YY}_{(\mathrm{reg})} = S^{YY}_{(\mathrm{none})} + 10^{-42}\ \mathrm{Hz}^{-1}, \tag{2.22b}$$
$$S^{ZZ}_{(\mathrm{reg})} = S^{ZZ}_{(\mathrm{none})} + 10^{-42}\ \mathrm{Hz}^{-1}. \tag{2.22c}$$

On the other hand, the CSDs do not change. The choice of $10^{-42}\ \mathrm{Hz}^{-1}$ for the 'secondary noise level' is chosen somewhat arbitrarily, while still ensuring that the secondary noise does not exceed the first order instrumental noise in line with expectation in literature. In any case, this noise model can be seen as producing a upper bound to the uncertainties and a lower bound to the SNR. All methods are demonstrated in Figure 2.4 through a plot for the PSD of the X-channel.

Prodding the Fisher Information Matrix (FIM)

Next, in order to first estimate the influence of unequal noise on LISA, the FIM will be used and compared for various cases where different orbit files are used, with case *EQ* using an orbit using equal arms and case *ESA* using the expected ESA orbit. In each case, the FIM will further be calculated with the AET channels in three instances: symmetric noise, asymmetric noise with the off-diagonals, and asymmetric noise with only the diagonals, noted as $(AET)_=$,

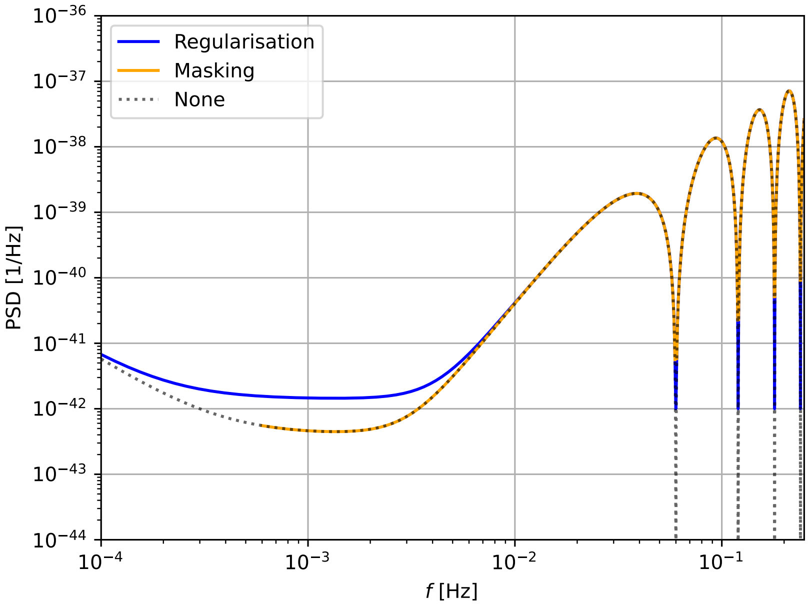

Figure 2.4: PSD graph for the Michelson variable X (using the symmetric noise model) to demonstrate each of the SNR methods.

$(AET)_{\neq}$, and $(AET)_{\neq}^{\mathrm{diag}}$ respectively. Checking for each of these cases allows us the estimate the effect of asymmetric noise as the off-diagonals are only present when the noise channels are asymmetric.

We can then further estimate the effect of the contribution of the asymmetric cross-correlations by comparing between $(AET)_{\neq}$, and $(AET)_{\neq}^{\mathrm{diag}}$. Each case will then be separated in whether it uses the expected orbit by ESA or an approximation in which the armlengths are kept equal and constant. Furthermore, the chosen SNR method used will be masking since it is the simplest method that still adheres to the noise models used in the literature.

MCMC posterior estimation

The last comparison one can finally make, is through calculating the full Bayesian posterior distributions in each case. This was initially attempted through combining the two packages `fastlisaresponse` and `Jim`, of which the former generates a full response for a given TDI-channel through a GPU-accelerated algorithm and the latter is a very fast MCMC sampler made for GW inference.(Wong et al. (2023); Wouters et al. (2024))
`Jim` had thus far only written code for ground-based GW detectors, so a new *space-based detector* class used with the code by `fastlisaresponse`.(Katz et al. (2022)) However, as will be described in more detail in the next chapter, there occurred compatibility issues between both packages and therefore a new code for the response generation was rewritten based on `fastlisaresponse`. This attempt also appeared to be the unfruitful and these shortcomings will be discussed as well.

Using JAX and its benefits

JAX is a Python library optimised for High-Performance Computing (HPC) with framework compatible for computations made with CPUs, GPUs, and TPUs.(JAX authors (2025b)) Specifically, this package was optimised for use in Machine Learning (ML). This package forms the basis for the numerical calculations made in Jim as it also exploits ML techniques as part of its optimisation. The benefits of JAX can be summarised to the following points:

- It forms a quick to learn, GPU-based alternative to perform NumPy-like calculations and operations with through `jax.numpy`;
- it contains a built-in 'Just-in-Time' compilation with `jax.jit`, which vastly improves the run time after compilation;
- It allows for easy parallelisation and vectorised calculations through functions such as `jax.vmap` and `jax.lax.scan`;
- It is capable of automatic differentiation through functions like `jax.grad` and `jax.hessian`.

Due to its benefits in automatic differentiation, a JAX-based code was also implemented in order to derive the FIM. All used code can be found in the following Github repository: https://github.com/KarelPletsStriker/jim/tree/using_flr1.0.2

Chapter 3

Results

Le vent se lève ! Il faut tenter de vivre !
- Paul Valéry

3.1 SNR comparisons

Examining first the effects on the SNR for all relevant cases, one can find the results in Table 3.1. SNR density - the relative contribution of each frequency to the SNR - is provided for each SNR method in Figure 3.1. From the onset, it is clear that the need for SNR methods is justified, with the lack of any method producing unphysical SNRs next to the fact that the SNRs for (XYZ) and (AET) do not correspond, even for the same noise model. One can further see that the SNR for the regularized noise model is significantly lower for the same channels and noise models.

SNR method	$(XYZ)_=$	$(XYZ)_{\neq}$	$(AET)_=$	$(AET)_{\neq}$
None	33.0	2.47×10^5	35.0	2.02×10^6
Masking	32.8	26.6	35.2	30.3
Regularisation	32.8	26.6	36.3	30.2

Table 3.1: Tabel displaying the SNRs for each channel and noise model, calculated with each SNR method. The input parameters were $(A, f_0, \dot{f}_0, \iota, \phi_0, \psi, \beta, \lambda) = (1.08 \times 10^{-22}, 25.0 \text{ mHz}, 1.50 \times 10^{-14} \text{ Hz}^2, 1.12 \text{ rad}, 4.9 \text{ rad}, 2.33 \text{ rad}, 0.92 \text{ rad}, 5.2 \text{ rad})$.

Furthermore, Figure 3.1 shows SNR density, i.e. the relative contribution of each frequency to the SNR for the same signal in each case. Noting first that $L \approx 8.340$ ls and therefore $1/2L \approx 60.0$ mHz, one can clearly see the periodic bumps at each TDI mode. This serves as another justification for the use of the proposed methods. However, one must note the strange discrepancies between the SNRs using the same noise model. As (XYZ) and (AET) are mere linear transformations of each other, it is notable they do not produce the same SNRs. This may be due to the fact the covariance matrices may still be ill-conditioned near the masked regions and therefore may sometimes produce negative values in the integrand to be negated. Since the masking method is the closest method currently used in the literature and more physically justifiable, for all further runs, this method is therefore chosen when calculating the FIM.

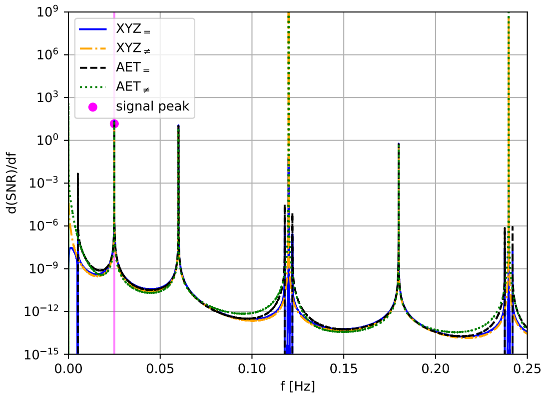

(a) No method

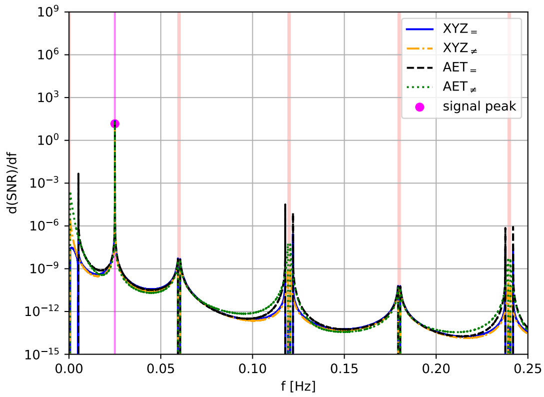

(b) Masking (red bars indicate masked regions)

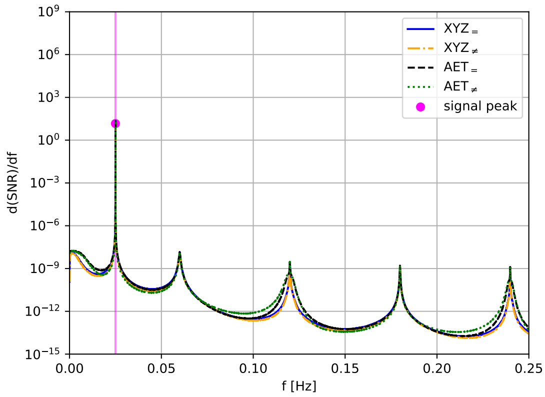

(c) Regularisation

Figure 3.1: Figure showing the SNR density with the various SNR methods. As the used waveform is also quasi-monochromatic, the peak frequency is also indicated.

3.2 Estimating the Fisher Information Matrix

One can find the (partial) covariance matrices for the extrinsic parameters $(\iota, \psi, \beta, \lambda)$ for each noise case in tables 3.2 and 3.3. Furthermore, the covariance is similarly visualised with the corresponding multivariate gaussian distribution in figures 3.2 and 3.3. For the intrinsic relevant parameters $(A,\ f_0,\ \dot{f}_0,\ \phi_0,\ \iota, \psi)$, there appeared to be numerical instabilities when attempting invert the FIM as it appears that for all cases and noise models the variance is nearly 0. This is to be expected as the waveform is quasi-monochromatic and therefore the integrand is approximately a Dirac delta. After excluding f_0, the table 3.4 and 3.5 and figures 3.4 and 3.5 show the covariance for the remaining intrinsic relevant parameters for case *EQ*.

Comparing the individual variances for each noise model, one can determine that on the symmetric and purely diagonal asymmetric noise models underestimate the variance for all variables except for the parameter. Taking the values of β in case *ESA* as an example, the variance of both diagonal noise models is by as much as 45% and 43% lower than the more accurate asymmetric model with off-diagonals. From this, one can infer that the diagonal models would produce biases when sampling the posterior using the 'incorrect' noise models.

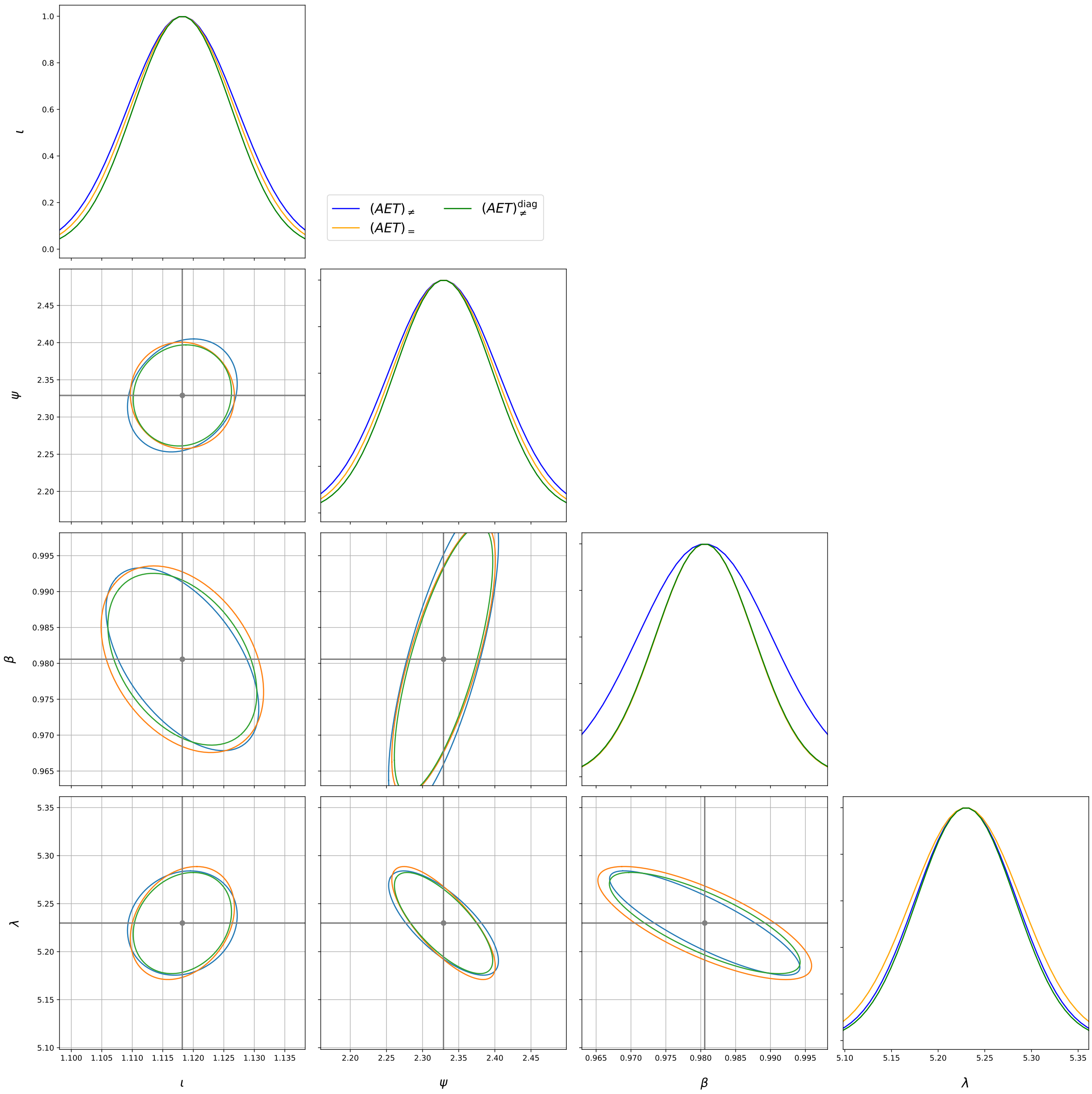

Figure 3.2: Covariance plot for extrinsic parameters for case EQ.

One can also compare the uncertainties for the intrinsic parameters as opposed to the intrinsic ones. From the visualisations, it appears the extrinsic parameters have a closer alignment amongst each other than the intrinsic ones. Indeed, if we compare the deviation in the variances for ι and ψ, we find that not only are they are consistently greater for the covariance matrix with the intrinsic parameters, but the correspondence between the noise models is also closer. For the diagonal noise models, both parameters underestimate the variance by 10-20% with the covariance for the extrinsic parameters as opposed to 30-40% with the intrinsic parameters. This is probably due to the fact the extrinsic parameters are much more strongly correlated, with ι and ψ even being nearly colinear with β, whereas they only exhibit this correlation with A.

$(AET)_{\neq}$	ι	ψ	β	λ
ι	8.133×10^{-5}	1.66×10^{-4}	-1.584×10^{-4}	5.036×10^{-5}
ψ	1.66×10^{-4}	5.956×10^{-3}	1.406×10^{-3}	-3.216×10^{-3}
β	-1.584×10^{-4}	1.406×10^{-3}	1.073×10^{-4}	-6.978×10^{-4}
λ	5.036×10^{-5}	-3.216×10^{-3}	-6.978×10^{-4}	3.021×10^{-3}
$(AET)_{\neq}^{\text{diag}}$	ι	ψ	β	λ
ι	6.487×10^{-5}	5.73×10^{-5}	-1.459×10^{-4}	7.66×10^{-5}
ψ	5.73×10^{-5}	4.854×10^{-3}	1.059×10^{-3}	-2.836×10^{-3}
β	-1.459×10^{-4}	1.059×10^{-3}	6.098×10^{-5}	-6.185×10^{-4}
λ	7.66×10^{-5}	-2.836×10^{-3}	-6.185×10^{-4}	2.815×10^{-3}
$(AET)_{=}$	ι	ψ	β	λ
ι	7.257×10^{-5}	5.197×10^{-6}	-1.729×10^{-4}	1.184×10^{-4}
ψ	5.197×10^{-6}	5.414×10^{-3}	1.132×10^{-3}	-3.398×10^{-3}
β	-1.729×10^{-4}	1.132×10^{-3}	5.864×10^{-5}	-7.473×10^{-4}
λ	1.184×10^{-4}	-3.398×10^{-3}	-7.473×10^{-4}	3.491×10^{-3}

Table 3.2: Covariance matrix for the extrinsic parameters in case *ESA*

$(AET)_{\neq}$	ι	ψ	β	λ
ι	8.084×10^{-5}	1.388×10^{-4}	-1.594×10^{-4}	7.005×10^{-5}
ψ	1.388×10^{-4}	5.769×10^{-3}	1.326×10^{-3}	-2.986×10^{-3}
β	-1.594×10^{-4}	1.326×10^{-3}	9.082×10^{-5}	-6.494×10^{-4}
λ	7.005×10^{-5}	-2.986×10^{-3}	-6.494×10^{-4}	2.947×10^{-3}
$(AET)_{\neq}^{\text{diag}}$	ι	ψ	β	λ
ι	6.485×10^{-5}	3.867×10^{-5}	-1.459×10^{-4}	9.272×10^{-5}
ψ	3.867×10^{-5}	4.62×10^{-3}	9.878×10^{-4}	-2.657×10^{-3}
β	-1.459×10^{-4}	9.878×10^{-4}	4.96×10^{-5}	-5.871×10^{-4}
λ	9.272×10^{-5}	-2.657×10^{-3}	-5.871×10^{-4}	2.772×10^{-3}
$(AET)_{=}$	ι	ψ	β	λ
ι	7.277×10^{-5}	-1.276×10^{-5}	-1.727×10^{-4}	1.377×10^{-4}
ψ	-1.276×10^{-5}	5.122×10^{-3}	1.056×10^{-3}	-3.215×10^{-3}
β	-1.727×10^{-4}	1.056×10^{-3}	4.897×10^{-5}	-7.197×10^{-4}
λ	1.377×10^{-4}	-3.215×10^{-3}	-7.197×10^{-4}	3.46×10^{-3}

Table 3.3: Covariance matrix for the extrinsic parameters in case *EQ*

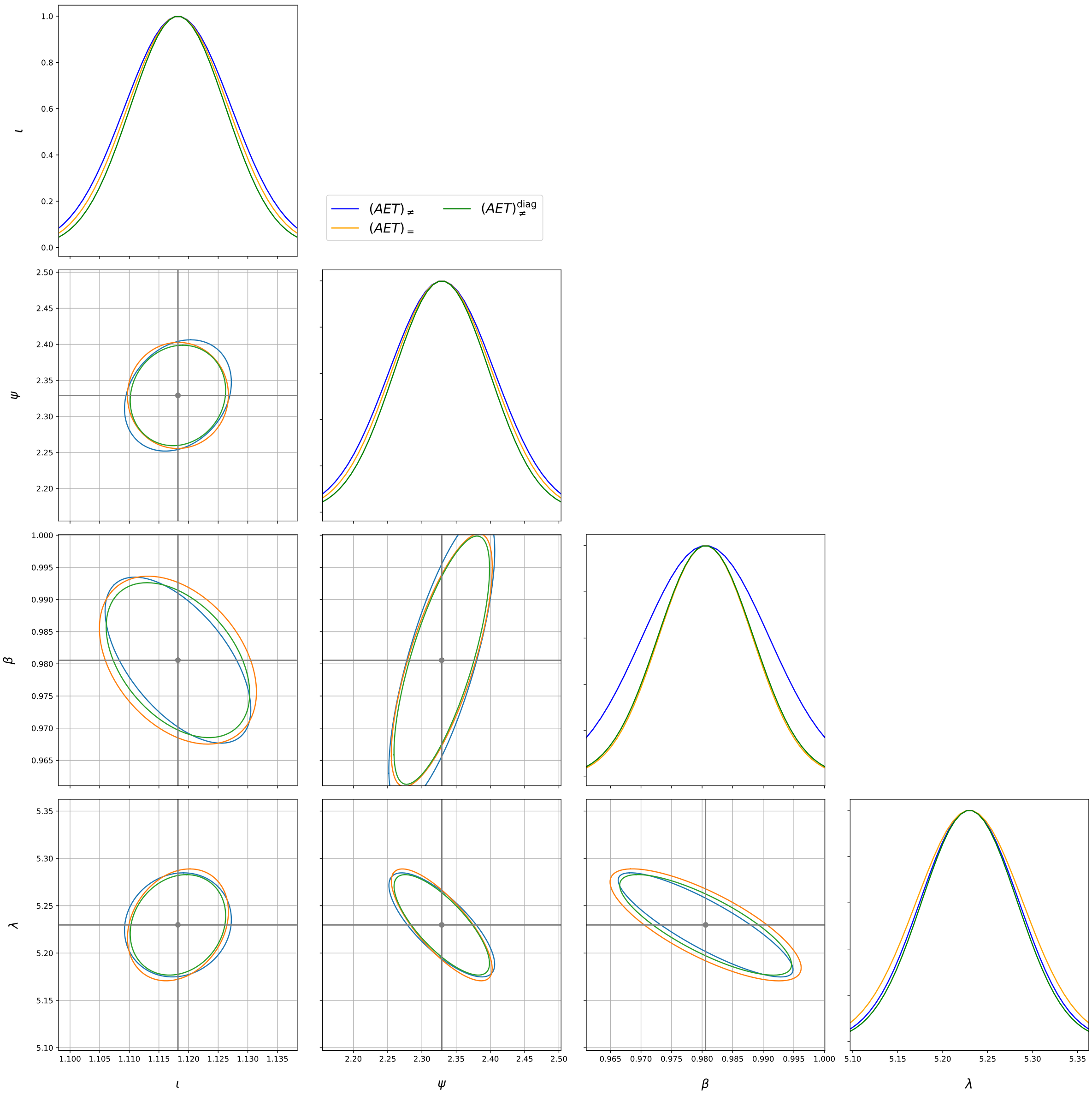

Figure 3.3: Covariance plot for extrinsic parameters for case ESA.

It is also noteworthy to mention the strong correspondence between both diagonal noise models. This is likely due to the fact the asymmetric noise parameters A_{ij} and P_{ij} average out to the symmetric noise parameters. As described in appendix A, the PSDs for the (AET) channels are themselves weighted averages of the PSDs and CSDs for the (XYZ) channels. Averaging these parameters out then roughly approximates the symmetric PSDs. This explanation would also be consistent with the conclusions made by (Hartwig et al. (2023)).

By examining the results between the two orbits through the relevant graphs, one can see that they match well, following the same patterns for predicted covariance. This implies that the difference in is purely a consequence of the noise model and not dependent on the orbit type.

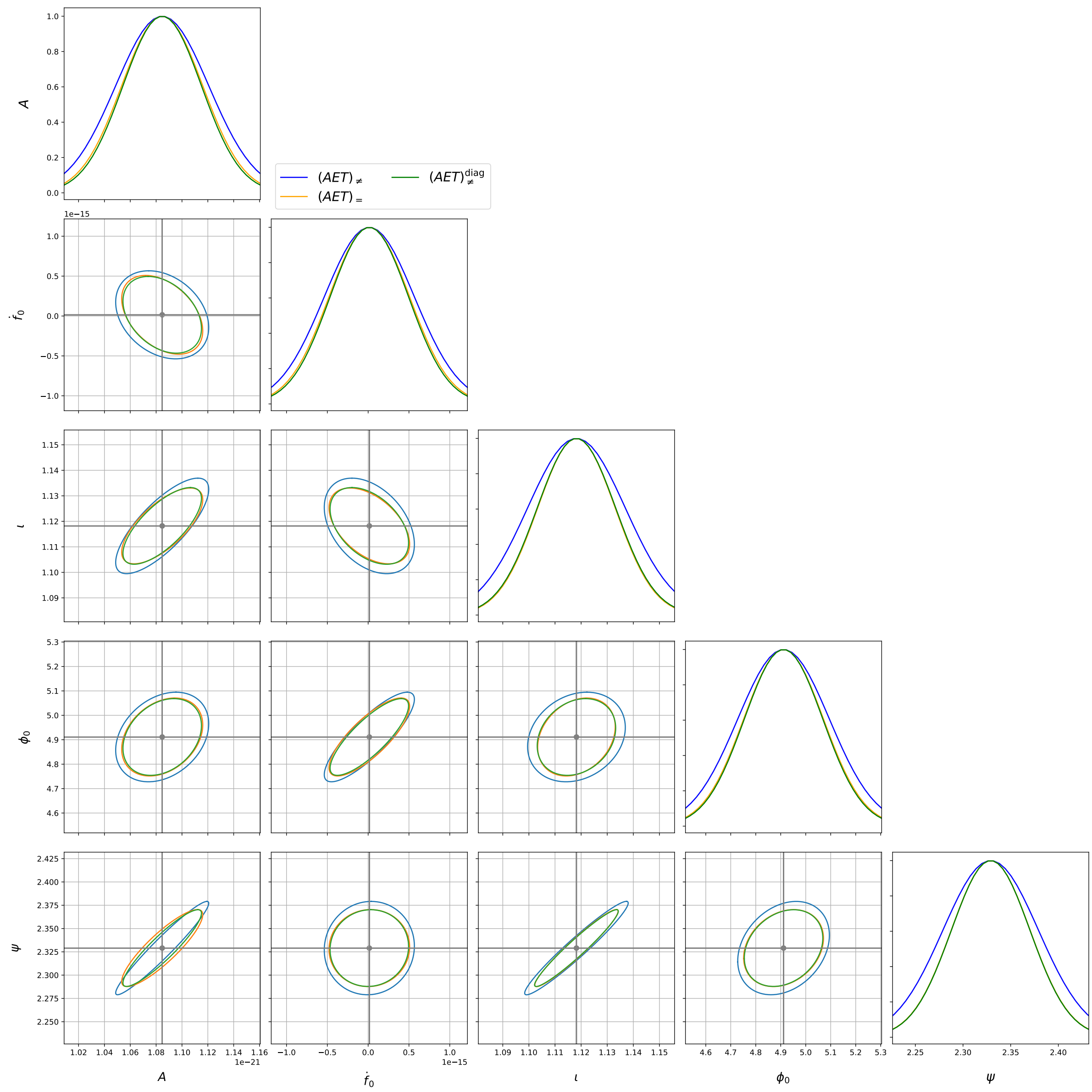

Figure 3.4: Covariance plot for intrinsic parameters for case *EQ*.

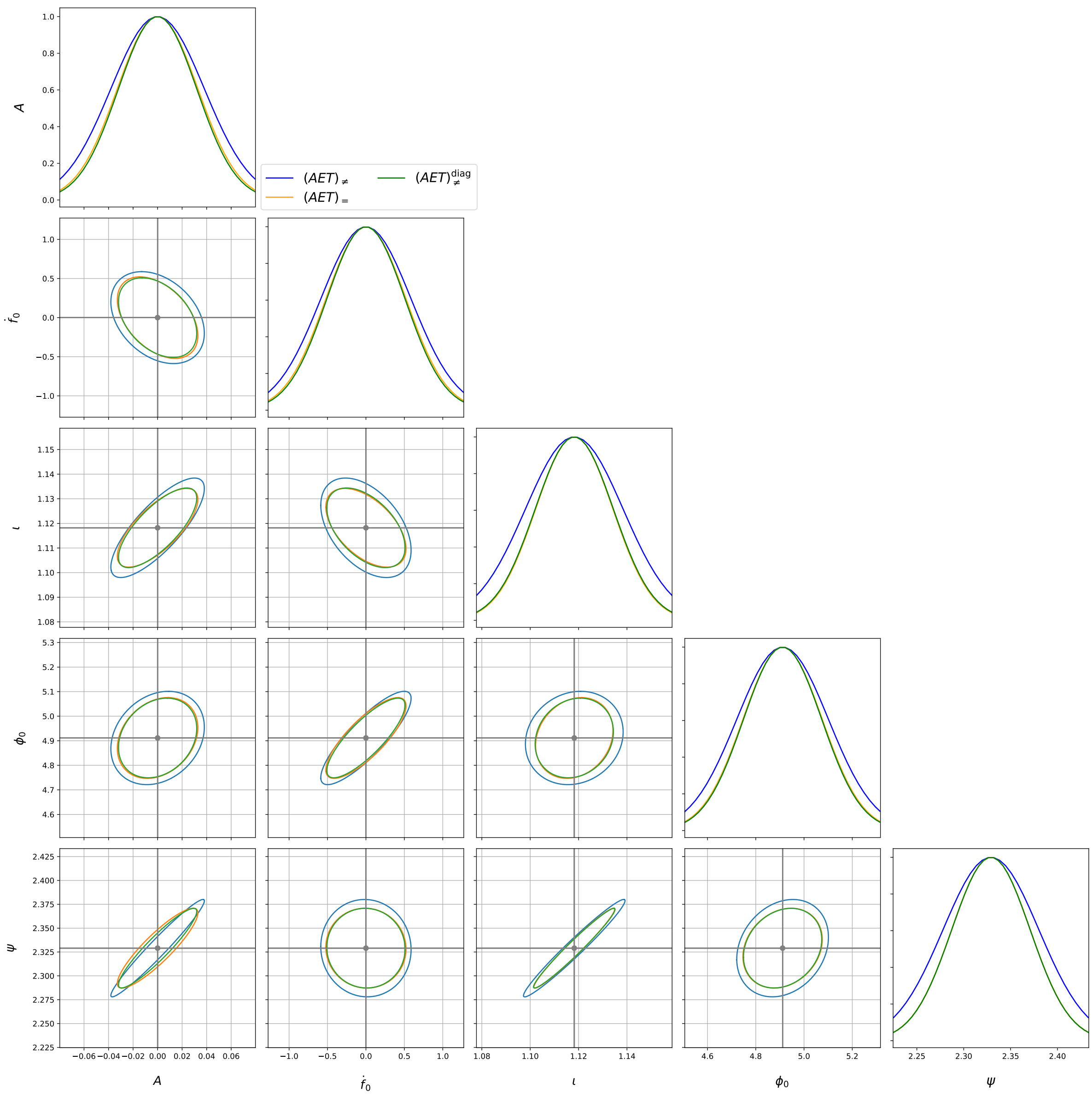

Figure 3.5: Covariance plot for intrinsic parameters for case *ESA*.

$(AET)_{\neq}$	A	$\dot{f}_0$	ι	ϕ_0	ψ
A	1.453×10^{-45}	-7.617×10^{-39}	6.072×10^{-25}	1.671×10^{-24}	1.888×10^{-24}
$\dot{f}_0$	-7.617×10^{-39}	3.454×10^{-31}	-5.38×10^{-18}	9.47×10^{-19}	-8.996×10^{-19}
ι	6.072×10^{-25}	-5.38×10^{-18}	4.083×10^{-4}	4.941×10^{-4}	1.059×10^{-3}
ϕ_0	1.671×10^{-24}	9.47×10^{-17}	4.941×10^{-4}	3.611×10^{-2}	2.178×10^{-3}
ψ	1.888×10^{-24}	-8.996×10^{-19}	1.059×10^{-3}	2.178×10^{-3}	2.604×10^{-3}
$(AET)_{\neq}^{\text{diag}}$	A	$\dot{f}_0$	ι	ϕ_0	ψ
A	1.018×10^{-45}	-6.44×10^{-39}	3.835×10^{-25}	1.24×10^{-24}	1.231×10^{-24}
$\dot{f}_0$	-6.44×10^{-39}	2.593×10^{-31}	-4.084×10^{-18}	6.791×10^{-17}	-4.357×10^{-19}
ι	3.835×10^{-25}	-4.084×10^{-18}	2.617×10^{-4}	4.059×10^{-4}	6.946×10^{-4}
ϕ_0	1.24×10^{-24}	6.791×10^{-17}	4.059×10^{-4}	2.63×10^{-2}	1.471×10^{-3}
ψ	1.231×10^{-24}	-4.357×10^{-19}	6.946×10^{-4}	1.471×10^{-3}	1.743×10^{-3}
$(AET)_{=}$	A	$\dot{f}_0$	ι	ϕ_0	ψ
A	1.079×10^{-45}	-7.52×10^{-39}	3.78×10^{-25}	1.388×10^{-24}	1.215×10^{-24}
$\dot{f}_0$	-7.52×10^{-39}	2.721×10^{-31}	-4.4×10^{-18}	6.815×10^{-17}	-4.987×10^{-19}
ι	3.78×10^{-25}	-4.4×10^{-18}	2.556×10^{-4}	4.965×10^{-4}	6.886×10^{-4}
ϕ_0	1.388×10^{-24}	6.815×10^{-17}	4.965×10^{-4}	2.704×10^{-2}	1.489×10^{-3}
ψ	1.215×10^{-24}	-4.987×10^{-19}	6.886×10^{-4}	1.489×10^{-3}	1.75×10^{-3}

Table 3.4: Covariance matrix for the intrinsic parameters in case *ESA*

$(AET)_{\neq}$	A	$\dot{f}_0$	ι	ϕ_0	ψ
A	1.296×10^{-45}	-5.727×10^{-39}	5.162×10^{-25}	1.955×10^{-24}	1.733×10^{-24}
$\dot{f}_0$	-5.727×10^{-39}	3.047×10^{-31}	-3.993×10^{-18}	8.517×10^{-17}	1.167×10^{-18}
ι	5.162×10^{-25}	-3.993×10^{-18}	3.506×10^{-4}	7.318×10^{-4}	9.749×10^{-4}
ϕ_0	1.955×10^{-24}	8.517×10^{-17}	7.318×10^{-4}	3.363×10^{-2}	2.527×10^{-3}
ψ	1.733×10^{-24}	1.167×10^{-18}	9.749×10^{-4}	2.527×10^{-3}	2.509×10^{-3}
$(AET)_{\neq}^{\text{diag}}$	A	$\dot{f}_0$	ι	ϕ_0	ψ
A	9.831×10^{-46}	-6.306×10^{-39}	3.224×10^{-25}	1.547×10^{-24}	1.125×10^{-24}
$\dot{f}_0$	-6.306×10^{-39}	2.438×10^{-31}	-3.52×10^{-18}	6.197×10^{-17}	6.54×10^{-19}
ι	3.224×10^{-25}	-3.52×10^{-18}	2.207×10^{-4}	6.253×10^{-4}	6.434×10^{-4}
ϕ_0	1.547×10^{-24}	6.197×10^{-17}	6.253×10^{-4}	2.549×10^{-2}	1.672×10^{-3}
ψ	1.125×10^{-24}	6.54×10^{-19}	6.434×10^{-4}	1.672×10^{-3}	1.706×10^{-3}
$(AET)_{=}$	A	$\dot{f}_0$	ι	ϕ_0	ψ
A	9.217×10^{-46}	-5.225×10^{-39}	3.273×10^{-25}	1.415×10^{-24}	1.137×10^{-24}
$\dot{f}_0$	-5.225×10^{-39}	2.311×10^{-31}	-3.188×10^{-18}	6.147×10^{-17}	7.986×10^{-19}
ι	3.273×10^{-25}	-3.188×10^{-18}	2.261×10^{-4}	5.504×10^{-4}	6.465×10^{-4}
ϕ_0	1.415×10^{-24}	6.147×10^{-17}	5.504×10^{-4}	2.466×10^{-2}	1.676×10^{-3}
ψ	1.137×10^{-24}	7.986×10^{-19}	6.465×10^{-4}	1.676×10^{-3}	1.695×10^{-3}

Table 3.5: Covariance matrix for the intrinsic parameters in case *EQ*

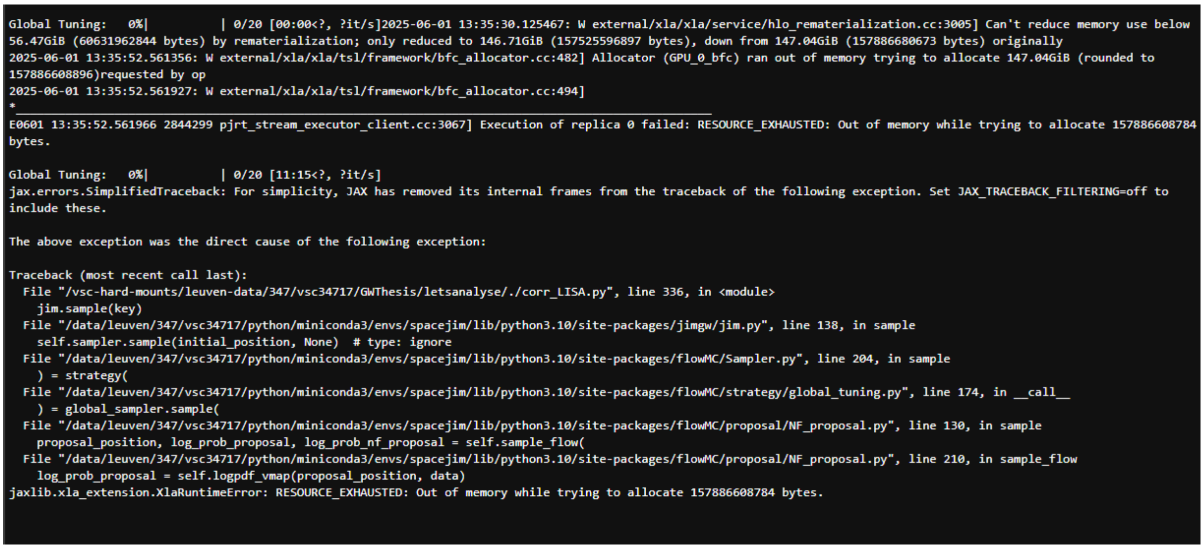

Figure 3.6: Screenshot of the aforementioned OOM error message

3.3 Attempting Parameter Estimation with `JIM`

As stated before, this part of the thesis project eventually turned out to be unsuccessful. Despite several attempts to mend these issues, it nevertheless turned out to be mostly in vain. First, it was discovered there were incompatibility issues between `Jim` and `fastlisaresponse`, more specifically through `JAX`. As `JIM` exploits `JAX`'s vectorisation and compilation features, it first examines the relevant functions by sending abstract variables as the input parameters, such as for the sampling and thus also response generation. `fastlisaresponse`'s `NumPy`- and `CuPy`-based code cannot interpret these abstract tracers, thus raising concretisation errors.(JAX authors (2025a)) Because of this, it is therefore impossible to create any code incorporating both `JIM` and `fastlisaresponse` to create a space-based detector class within the same framework.

However, it is still possible to create the space-based detector class with the response generation if one is able to rewrite all of `fastlisaresponse` with `JAX`, turning the equations (2.1), (2.5), (2.12) and (2.16) into Python code and applying Lagrange interpolation where applicable, analogous to `fastlisaresponse`. This attempt can also be found in the aforementioned Github repository. Nevertheless, while it did become possible to generate waveforms within reasonable time, issues still remained, making it impossible for properly implement the space-based detector within the time frame of this thesis project. To be specific, in spite of attempts made to balance the memory usage with computation time, the code kept on running into Out of Memory (OOM) errors, such as the one shown in Figure 3.6. It is suspected these errors are a result from each signal - which are stored as double-precision arrays with sizes on the order of tens of millions points - is improperly deleted when attempting to sample with `JIM`. Due to the time constraints of this master thesis project, it was not possible to find out the true cause of this error, nor to correct it.

Chapter 4

Conclusions

In this thesis project, the effects of asymmetric noise were examined for LISA. While proper PE was not achieved, it was nevertheless possible to assess the effects by proxy through viewing the SNR and comparing the FIM between various cases. Through the SNR results we were able to develop simple methods to handle the TDI artifacts and maintain reasonable and consistent values. Finally, the failed attempt at developing a fast posterior sampler for `JIM` was described and discussed.

While a full analysis and PE did not turn out possible within the current timeline, the FIM analysis indicated a symmetric or diagonal noise model would underestimate the uncertainties by a significant degree. This would then imply that when analysing LISA signals, biases could arise if the proper noise model is not applied. Nevertheless, this could only be inferred through the FIM and this would only be possible by properly sampling a posterior distribution for a noisy signal. Furthermore, another consequence of this project was determine the applicability of the quasi-orthogonal (AET) channel, which relies on the symmetry of the various noise channels *and* armlengths, of which the latter is definitely known not to apply. It is therefore evident to say the (AET) variables have only a limited usage in the real case seeing as it does not approximate the asymmetric values as well as is desirable.

In conclusion, despite not fully confirming the hypothesis, this thesis project was able to effectively indicate the dangers of asymmetric noise for LISA whether it is applies to the calculation of the SNR or the assessment of the uncertainties through the FIM.

Suggestions for future research

For future projects, it will first be fruitful to determine the effects of asymmetric noise and different orbits on PE. Then one can actually see what possible biases could come out as well as the uncertainties. As has been discussed in (Hartwig et al. (2023)) and (Katz et al. (2022)), it is guaranteed the noise levels as well as the orbit of LISA will be asymmetric. Nonetheless, the goal of developing a fast MCMC sampler for LISA remains a challenge in spite of the hopes at the start of this project. Due to the differences between ground-based detectors such as ET and space-based detectors such as LISA, it will not be trivial to simply emulate a sampler optimised for one type to a sampler applicable for the other without forethought. Particularly since the sources expected for LISA are much longer and will therefore also require signals with points on the order of tens of millions, the parallelisation may work adversely by consuming too much memory as demonstrated by the aforementioned errors. It is suspected Python has a more difficult time deleting memory allocated by `JAX` variables, which could be investigated further.

Furthermore, it would also be useful to perform the same analyses for other types of signals - more notably MBHBs and EMRIs, which are known to have a more spread-out contribution to the SNR as opposed to the near-monochromatic GBs - or other types of channels such as the Sagnac variables which are known to have no TDI artifacts for $f \lesssim 120\ \mathrm{mHz}$.[1](Hartwig and Muratore (2022)) One would then expect the Sagnac variables be less affected by the SNR methods. It would also be a quick and easy comparison to expand the FIM calculations to these variables as well. Given how the waveform parameters were not as affected by the different noise models as the spatial parameters. Given how important sky localisation is for much of LISA's science goals, it is nevertheless important to therefore correctly verify whether the localisation is as troublesome for different types of sources as well.

Finally, despite the recent work by (Cireddu et al. (2024)), it remains unclear how a triangular ET would be affected for asymmetric noise. As this thesis has shown, the asymmetry does have an effect on both the SNR and FIM calculations. Since it is also expected ET's correlated noise will be asymmetric, it could be fruitful to assess the potential biases brought upon. This endeavour may be less worthwhile, though, seeing as it is expected that ET's PSDs and CSDs will vary over time, like LVK. As general networks of correlated detectors tend to have asymmetric correlations as well, symmetry is often used as an approximation without issue. Nonetheless, it may be an interesting research topic to verify the lack of influence due to asymmetry.

[1]More exactly, this corresponds to the second TDI mode for the Michelson variables.

Bibliography

Abac, A., Abramo, R., Albanesi, S., Albertini, A., Agapito, A., Agathos, M., Albertus, C., Andersson, N., Andrade, T., Andreoni, I., Angeloni, F., Antonelli, M., Antoniadis, J., Antonini, F., Sedda, M. A., Artale, M. C., Ascenzi, S., Auclair, P., Bachetti, M., Badger, C., Banerjee, B., Barba-González, D., Barta, D., Bartolo, N., Bauswein, A., Begnoni, A., Beirnaert, F., Bejger, M., Belgacem, E., Bellomo, N., Bernard, L., Bernardini, M. G., Bernuzzi, S., Berry, C. P. L., Berti, E., Bertone, G., Bettoni, D., Bezares, M., Bhagwat, S., Bisero, S., Bizouard, M. A., Blanco-Pillado, J. J., Blasi, S., Bonino, A., Borghese, A., Borghi, N., Borhanian, S., Bortolas, E., Botticella, M. T., Branchesi, M., Breschi, M., Brito, R., Brocato, E., Broekgaarden, F. S., Bulik, T., Buonanno, A., Burgio, F., Burrows, A., Calcagni, G., Canevarolo, S., Cappellaro, E., Capurri, G., Carbone, C., Casadio, R., Cayuso, R., Cerdá-Durán, P., Char, P., Chaty, S., Chiarusi, T., Chruslinska, M., Cireddu, F., Cole, P., Colombo, A., Colpi, M., Compère, G., Contaldi, C., Corman, M., Crescimbeni, F., Cristallo, S., Cuoco, E., Cusin, G., Canton, T. D., Dálya, G., D'Avanzo, P., Davari, N., Luca, V. D., Renzis, V. D., Valle, M. D., Pozzo, W. D., Santi, F. D., Santis, A. L. D., Dietrich, T., Dimastrogiovanni, E., Domenech, G., Doneva, D., Drago, M., Dupletsa, U., Duval, H., Dvorkin, I., Elias-Rosa, N., Fairhurst, S., Fantina, A. F., Fasiello, M., Fays, M., Fender, R., Fischer, T., Foucart, F., Fragos, T., Foffa, S., Franciolini, G., Gair, J., Gamba, R., Garcia-Bellido, J., García-Quirós, C., Árpád Gergely, L., Ghirlanda, G., Ghosh, A., Giacomazzo, B., Gittins, F., Giudice, I. F., Goncharov, B., Gonzalez, A., Goriély, S., Graziani, L., Greco, G., Gualtieri, L., Guidi, G. M., Gupta, I., Haney, M., Hannam, M., Harms, J., Harutyunyan, A., Haskell, B., Haungs, A., Hazra, N., Hemming, G., Heng, I. S., Hinderer, T., van der Horst, A., Hu, Q., Husa, S., Iacovelli, F., Illuminati, G., Inguglia, G., Villalba, D. I., Janquart, J., Janssens, K., Jenkins, A. C., Jones, I., Kacskovics, B., Klessen, R. S., Kokkotas, K., Kuan, H.-J., Kumar, S., Kuroyanagi, S., Laghi, D., Lamberts, A., Lambiase, G., Larrouturou, F., Leaci, P., Lenzi, M., Levan, A., Li, T. G. F., Li, Y., Liang, D., Limongi, M., Liu, B., Llanes-Estrada, F. J., Loffredo, E., Long, O., Lope-Oter, E., Lukes-Gerakopoulos, G., Maggio, E., Maggiore, M., Mancarella, M., Mapelli, M., Marchant, P., Margiotta, A., Mariotti, A., Marriott-Best, A., Marsat, S., Martínez-Pinedo, G., Maselli, A., Mastrogiovanni, S., Matos, I., Melandri, A., Mendes, R. F. P., de Souza, J. M. S., Mentasti, G., Mezcua, M., Mösta, P., Mondal, C., Moresco, M., Mukherjee, T., Muttoni, N., Nagar, A., Narola, H., Nava, L., Moreno, P. N., Nelemans, G., Nissanke, S., Obergaulinger, M., Oertel, M., Oganesyan, G., Onori, F., Pacilio, C., Pagliaroli, G., Palomba, C., Pang, P. T. H., Pani, P., Papalini, L., Patricelli, B., Patruno, A., Pedrotti, A., Perego, A., Pérez-García, M. A., Périgois, C., Perna, G., Pérox, C., Perret, J., Perrodin, D., Pesci, A., Pfeiffer, H. P., Piccinni, O. J., Pieroni, M., Piranomonte, S., Pompili, L., Porter, E. K., Porto, R. A., Pound, A., Powell, J., Puech, M., Pratten, G., Puecher, A., Pujolas, O., Quartin, M., Raduta, A. R., Ramos-Buades, A., Rase, A., Razzano, M., Rea, N., Regimbau, T., Renzini, A., Rettegno, P., Ricciardone, A., Riotto, A., Romero-Rodriguez, A., Ronchini, S., Rosinska, D., Rossi, A., Roy, S., Rubiera-Garcia, D., Rubio, J., Ruiz-Lapuente, P., Sagun, V., Sakellariadou, M., Salafia, O. S., Samajdar, A., Sanchis-Gual, N., Sanna, A., Santoliquido, F., Sathyaprakash, B., Schmidt, P., Schmidt, S., Schneider, F. R. N., Schneider, R., Sedrakian, A., Servant, G., Sevrin, A., Shao, L., Silva, H. O., Simakachorn, P., Smartt, S., Sotiriou, T. P., Spera, M., Stamerra, A., Steer, D. A., Steinhoff, J., Stergioulas, N., Sturani, R., Suárez, D., Suresh, J., Swain, S., Tagliazucchi, M., Tamanini, N., Tasinato, G., Tauris, T. M., Tissino, J., Tomaselli, G. M., Toonen, S., Torres-Forné, A., Turski, C., Ugolini, C., Vagenas, E. C., Dall'Armi, L. V., Valenti, E., Valiante, R., Broeck, C. V. D., van de Meent, M., van Son, L. A. C., Vanvlasselaer, M., Vaglio, M., Varma, V., Veitch, J., Vaskonen, V., Vergani, S. D., Wils, M., Witek, H., Wong, I. C. F., Yazadjiev, S., Yim, G., Acernese, F., Ahn, H., Allocca, A., Amato, A., Andrés-Carcasona, M., Avallone, G., Bachlechner, M., Baer, P., Bagnasco, S., Balbi, G., Barone, F., Benedetti, E., Benning, C., Bini, S., Salcedo, J. L. B., Bozza, V., Bruno, M., Butz, T., Califano, M., Calloni, E., Carapella, G., Cardini, A., Subrahmanya, S. C., Chiadini, F., Chiummo, A., Cianetti, S., Ciani, G., Coccia, E., Contu, A., Cozzumbo, A., Croney, L., Crosta, M., D'Agostino, R., Danilishin, S., D'Antonio, S., Bolle, J. D., Degallaix, J., Laurentis, M. D., della Monica, R., Marco, F. D., de Martino, I., Rosa, R. D., Salvo, R. D., Simone, R. D., Detavernier, C., Diaferia, G., Cesare, M. D., Fiore, L. D., Giovanni, M. D., Pace, S. D., Docherty, J., D'Urso, D., Mecherfi, O. E., Errico, L., Fabrizi, F., Fafone, V., Fanti, V., Fittipaldi, R., Fiumara, V., Freise, A., Funk, S., Gaedtke, M., Garufi, F., Gerberding, O., Giangrandi, E., Giunchi, C., Graham, V., Granata, M., Granata, V., Green, A., Haughian, K., Heisenberg, L., Hennig, M., Hild, S., Hoang, V. L., Holland, N., Iannone, G., Isleif, K.-S., Joppe, R., Kim, C.-H., Kim, C., Kim, K., Korb, E., Korobko, M., Kranzhoff, L., Kuhlbusch, T., Lacaille, G., Lartaux-Vollard, A., Lavezzi, L., Laycock, P., Lee, S., Lee, S., Lee, S., Losurdo, G., Lucchesi, L., Lück, H., Macquet, A., Majorana, E., Mangano, V., Martelli, F., Martin, I., Martinez, M., Masoni, A., Massaro, L., Melini, D., Mercurio, A., Mereni, L., Miller, A. L., Mirasola, L., Mitchell, A., Molinari, I., Montani, M., Mow-Lowry, C., Murgia, R., Murray, P. G., Muscas, G., Naticchioni, L., Nela, A., Nery, M., Niggemann, T., Nippe, N., Novak, J., Numic, A., Olivieri, M., Orsini, M., Park, J. G., Pascucci, D., Perreca, A., Piergiovanni, F., Pierro, V., Pinard, L., Pinto, I., Punturo, M., Puppo, P., Quochi, F., Rading, R. O., Rapagnani, P., Ricci, M., Rodrigues, D., Romano, R., Rozza, D., Saffarieh, P., Santucci, F., Schramm, S., Schwab, B., Sequino, V., Neto, L. S., Silenzi, L., Sintes, A. M., Sopuerta, C. F., Spencer, A., Stahl, A., Steinlechner, J., Steinlechner, S., Szabó, R., Thümmler, T., Torniamenti, S., Travaglini, R., Trozzo, L., Vaccaro, M. P., Valentini, M., Ván, P., van Dongen, J., van Heijningen, J., van Ranst, Z., Vardaro, M., Verdier, P., Vernieri, D., Wagner, N., Woehler, J., Wolf, J., Zavattini, G., Zink, A., and Zmija, A. (2025). The science of the einstein telescope.

Abbott, B. P., Abbott, R., Abbott, T. D., Abernathy, M. R., Acernese, F., Ackley, K., Adams, C., Adams, T., Addesso, P., Adhikari, R. X., Adya, V. B., Affeldt, C., Agathos, M., Agatsuma, K., Aggarwal, N., Aguiar, O. D., Aiello, L., Ain, A., Ajith, P., Allen, B., Allocca, A., Altin, P. A., Anderson, S. B., Anderson, W. G., Arai, K., Araya, M. C., Arceneaux, C. C., Areeda, J. S., Arnaud, N., Arun, K. G., Ascenzi, S., Ashton, G., Ast, M., Aston, S. M., Astone, P., Aufmuth, P., Aulbert, C., Babak, S., Bacon, P., Bader, M. K. M., Baker, P. T., Baldaccini, F., Ballardin, G., Ballmer, S. W., Barayoga, J. C., Barclay, S. E., Barish, B. C., Barker, D., Barone, F., Barr, B., Barsotti, L., Barsuglia, M., Barta, D., Bartlett, J., Bartos, I., Bassiri, R., Basti, A., Batch, J. C., Baune, C., Bavigadda, V., Bazzan, M., Behnke, B., Bejger, M., Bell, A. S., Bell, C. J., Berger, B. K., Bergman, J., Bergmann, G., Berry, C. P. L., Bersanetti, D., Bertolini, A., Betzwieser, J., Bhagwat, S., Bhandare, R., Bilenko, I. A., Billingsley, G., Birch, J., Birney, I. A., Birnholtz, O., Biscans, S., Bisht, A., Bitossi, M., Biwer, C., Bizouard, M. A., Blackburn, J. K., Blair, C. D., Blair, D. G., Blair, R. M., Bloemen, S., Bock, O., Bodiya, T. P., Boer, M., Bogaert, G., Bogan, C., Bohe, A., Bojtos, P., Bond, C., Bondu, F., Bonnand, R., Boom, B. A., Bork, R., Boschi, V., Bose, S., Bouffanais, Y., Bozzi, A., Bradaschia, C., Brady, P. R., Braginsky, V. B., Branchesi, M., Brau, J. E., Briant, T., Brillet, A., Brinkmann, M., Brisson, V., Brockill, P., Brooks, A. F., Brown, D. A., Brown, D. D., Brown, N. M., Buchanan, C. C., Buikema, A., Bulik, T., Bulten, H. J., Buonanno, A., Buskulic, D., Buy, C., Byer, R. L., Cadonati, L., Cagnoli, G., Cahillane, C., Bustillo, J. C., Callister, T., Calloni, E., Camp, J. B., Cannon, K. C., Cao, J., Capano, C. D., Capocasa, E., Carbognani, F., Caride, S., Diaz, J. C., Casentini, C., Caudill, S., Cavaglià, M., Cavalier, F., Cavalieri, R., Cella, G., Cepeda, C. B., Baiardi, L. C., Cerretani, G., Cesarini, E., Chakraborty, R., Chalermsongsak, T., Chamberlin, S. J., Chan, M., Chao, S., Charlton, P., Chassande-Mottin, E., Chen, H. Y., Chen, Y., Cheng, C., Chincarini, A., Chiummo, A., Cho, H. S., Cho, M., Chow, J. H., Christensen, N., Chu, Q., Chua, S., Chung, S., Ciani, G., Clara, F., Clark, J. A., Cleva, F., Coccia, E., Cohadon, P.-f., Colla, A., Collette, C. G., Cominsky, L., Constancio, M., Conte, A., Conti, L., Cook, D., Corbitt, T. R., Cornish, N., Corsi, A., Cortese, S., Costa, C. A., Coughlin, M. W., Coughlin, S. B., Coulon, J.-p., Countryman, S. T., Couvares, P., Cowan, E. E., Coward, D. M., Cowart, M. J., Coyne, D. C., Coyne, R., Craig, K., Creighton, J. D. E., Cripe, J., Crowder, S. G., Cumming, A., Cunningham, L., Cuoco, E., Canton, T. D., Danilishin, S. L., D'Antonio, S., Danzmann, K., Darman, N. S., Dattilo, V., Dave, I., Daveloza, H. P., Davier, M., Davies, G. S., Daw, E. J., Day, R., DeBra, D., Debreczeni, G., Degallaix, J., De Laurentis, M., Deléglise, S., Del Pozzo, W., Denker, T., Dent, T., Dereli, H., Dergachev, V., De Rosa, R., DeRosa, R. T., DeSalvo, R., Devine, C., Dhurandhar, S., Díaz, M. C., Di Fiore, L., Di Giovanni, M., Di Lieto, A., Di Pace, S., Di Palma, I., Di Virgilio, A., Dojcinoski, G., Dolique, V., Donovan, F., Dooley, K. L., Doravari, S., Douglas, R., Downes, T. P., Drago, M., Drever, R. W. P., Driggers, J. C., Du, Z., Ducrot, M., Dwyer, S. E., Edo, T. B., Edwards, M. C., Effler, A., Eggenstein, H.-b., Ehrens, P., Eichholz, J., Eikenberry, S. S., Engels, W., Essick, R. C., Etienne, Z., Etzel, T., Evans, M., Evans, T. M., Everett, R., Factourovich, M., Fafone, V., Fair, H., Fairhurst, S., Fan, X., Fang, Q., Farinon, S., Farr, B., Farr, W. M., Fauchon-Jones, E., Favata, M., Fays, M., Fehrmann, H., Fejer, M. M., Ferrante, I., Ferreira, E. C., Ferrini, F., Fidecaro, F., Fiori, I., Fiorucci, D., Fisher, R. P., Flaminio, R., Fletcher, M., Fournier, J.-d., Franco, S., Frasca, S., Frasconi, F., Frei, Z., Freise, A., Frey, R., Frey, V., Fricke, T. T., Fritschel, P., Frolov, V. V., Fulda, P., Fyffe, M., Gabbard, H. A. G., Gaebel, S. M., Gair, J. R., Gammaitoni, L., Gaonkar, S. G., Garufi, F., Gatto, A., Gaur, G., Gehrels, N., Gemme, G., Gendre, B., Genin, E., Gennai, A., George, J., Gergely, L., Germain, V., Ghosh, A., Ghosh, S., Giaime, J. A., Giardina, K. D., Giazotto, A., Gill, K., Glaefke, A., Goetz, E., Goetz, R., Gondan, L., González, G., Castro, J. M. G., Gopakumar, A., Gordon, N. A., Gorodetsky, M. L., Gossan, S. E., Gosselin, M., Gouaty, R., Graef, C., Graff, P. B., Granata, M., Grant, A., Gras, S., Gray, C., Greco, G., Green, A. C., Groot, P., Grote, H., Grunewald, S., Guidi, G. M., Guo, X., Gupta, A., Gupta, M. K., Gushwa, K. E., Gustafson, E. K., Gustafson, R., Hacker, J. J., Hall, B. R., Hall, E. D., Hammond, G., Haney, M., Hanke, M. M., Hanks, J., Hanna, C., Hannam, M. D., Hanson, J., Hardwick, T., Harms, J., Harry, G. M., Harry, I. W., Hart, M. J., Hartman, M. T., Haster, C.-j., Haughian, K., Healy, J., Heidmann, A., Heintze, M. C., Heitmann, H., Hello, P., Hemming, G., Hendry, M., Heng,

I. S., Hennig, J., Heptonstall, A. W., Heurs, M., Hild, S., Hoak, D., Hodge, K. A., Hofman, D., Hollitt, S. E., Holt, K., Holz, D. E., Hopkins, P., Hosken, D. J., Hough, J., Houston, E. A., Howell, E. J., Hu, Y. M., Huang, S., Huerta, E. A., Huet, D., Hughey, B., Husa, S., Huttner, S. H., Huynh-Dinh, T., Idrisy, A., Indik, N., Ingram, D. R., Inta, R., Isa, H. N., Isac, J.-m., Isi, M., Islas, G., Isogai, T., Iyer, B. R., Izumi, K., Jacqmin, T., Jang, H., Jani, K., Jaranowski, P., Jawahar, S., Jiménez-Forteza, F., Johnson, W. W., Johnson-McDaniel, N. K., Jones, D. I., Jones, R., Jonker, R. J. G., Ju, L., K, H., Kalaghatgi, C. V., Kalogera, V., Kandhasamy, S., Kang, G., Kanner, J. B., Karki, S., Kasprzack, M., Katsavounidis, E., Katzman, W., Kaufer, S., Kaur, T., Kawabe, K., Kawazoe, F., Kéfélian, F., Kehl, M. S., Keitel, D., Kelley, D. B., Kells, W., Kennedy, R., Key, J. S., Khalaidovski, A., Khalili, F. Y., Khan, I., Khan, S., Khan, Z., Khazanov, E. A., Kijbunchoo, N., Kim, C., Kim, J., Kim, K., Kim, N.-G., Kim, N., Kim, Y.-m., King, E. J., King, P. J., Kinzel, D. L., Kissel, J. S., Kleybolte, L., Klimenko, S., Koehlenbeck, S. M., Kokeyama, K., Koley, S., Kondrashov, V., Kontos, A., Korobko, M., Korth, W. Z., Kowalska, I., Kozak, D. B., Kringel, V., Krishnan, B., Królak, A., Krueger, C., Kuehn, G., Kumar, P., Kuo, L., Kutynia, A., Lackey, B. D., Landry, M., Lange, J., Lantz, B., Lasky, P. D., Lazzarini, A., Lazzaro, C., Leaci, P., Leavey, S., Lebigot, E. O., Lee, C. H., Lee, H. K., Lee, H. M., Lee, K., Lenon, A., Leonardi, M., Leong, J. R., Leroy, N., Letendre, N., Levin, Y., Levine, B. M., Li, T. G. F., Libson, A., Littenberg, T. B., Lockerbie, N. A., Logue, J., Lombardi, A. L., London, L. T., Lord, J. E., Lorenzini, M., Loriette, V., Lormand, M., Losurdo, G., Lough, J. D., Lousto, C. O., Lovelace, G., Lück, H., Lundgren, A. P., Luo, J., Lynch, R., Ma, Y., MacDonald, T., Machenschalk, B., MacInnis, M., Macleod, D. M., Magaña-Sandoval, F., Magee, R. M., Mageswaran, M., Majorana, E., Maksimovic, I., Malvezzi, V., Man, N., Mandel, I., Mandic, V., Mangano, V., Mansell, G. L., Manske, M., Mantovani, M., Marchesoni, F., Marion, F., Márka, S., Márka, Z., Markosyan, A. S., Maros, E., Martelli, F., Martellini, L., Martin, I. W., Martin, R. M., Martynov, D. V., Marx, J. N., Mason, K., Masserot, A., Massinger, T. J., Masso-Reid, M., Matichard, F., Matone, L., Mavalvala, N., Mazumder, N., Mazzolo, G., McCarthy, R., McClelland, D. E., McCormick, S., McGuire, S. C., McIntyre, G., McIver, J., McManus, D. J., McWilliams, S. T., Meacher, D., Meadors, G. D., Meidam, J., Melatos, A., Mendell, G., Mendoza-Gandara, D., Mercer, R. A., Merilh, E., Merzougui, M., Meshkov, S., Messenger, C., Messick, C., Meyers, P. M., Mezzani, F., Miao, H., Michel, C., Middleton, H., Mikhailov, E. E., Milano, L., Miller, J., Millhouse, M., Minenkov, Y., Ming, J., Mirshekari, S., Mishra, C., Mitra, S., Mitrofanov, V. P., Mitselmakher, G., Mittleman, R., Moggi, A., Mohan, M., Mohapatra, S. R. P., Montani, M., Moore, B. C., Moore, C. J., Moraru, D., Moreno, G., Morriss, S. R., Mossavi, K., Mours, B., Mow-Lowry, C. M., Mueller, C. L., Mueller, G., Muir, A. W., Mukherjee, A., Mukherjee, D., Mukherjee, S., Mukund, N., Mullavey, A., Munch, J., Murphy, D. J., Murray, P. G., Mytidis, A., Nardecchia, I., Naticchioni, L., Nayak, R. K., Necula, V., Nedkova, K., Nelemans, G., Neri, M., Neunzert, A., Newton, G., Nguyen, T. T., Nielsen, A. B., Nissanke, S., Nitz, A., Nocera, F., Nolting, D., Normandin, M. E., Nuttall, L. K., Oberling, J., Ochsner, E., O'Dell, J., Oelker, E., Ogin, G. H., Oh, J. J., Oh, S. H., Ohme, F., Oliver, M., Oppermann, P., Oram, R. J., O'Reilly, B., O'Shaughnessy, R., Ottaway, D. J., Ottens, R. S., Overmier, H., Owen, B. J., Pai, A., Pai, S. A., Palamos, J. R., Palashov, O., Palomba, C., Pal-Singh, A., Pan, H., Pan, Y., Pankow, C., Pannarale, F., Pant, B. C., Paoletti, F., Paoli, A., Papa, M. A., Paris, H. R., Parker, W., Pascucci, D., Pasqualetti, A., Passaquieti, R., Passuello, D., Patricelli, B., Patrick, Z., Pearlstone, B. L., Pedraza, M., Pedurand, R., Pekowsky, L., Pele, A., Penn, S., Perreca, A., Pfeiffer, H. P., Phelps, M., Piccinni, O., Pichot, M., Piergiovanni, F., Pierro, V., Pillant, G., Pinard, L., Pinto, I. M., Pitkin, M., Poggiani, R., Popolizio, P., Post, A., Powell, J., Prasad, J., Predoi, V., Premachandra, S. S., Prestegard, T., Price, L. R., Prijatelj, M., Principe, M., Privitera, S., Prodi, G. A., Prokhorov, L., Puncken, O., Punturo, M., Puppo, P., Pürrer, M., Qi, H., Qin, J., Quetschke, V., Quintero, E. A., Quitzow-James, R., Raab, F. J., Rabeling, D. S., Radkins, H., Raffai, P., Raja, S., Rakhmanov, M., Rapagnani, P., Raymond, V., Razzano, M., Re, V., Read, J., Reed, C. M., Regimbau, T., Rei, L., Reid, S., Reitze, D. H., Rew, H., Reyes, S. D., Ricci, F., Riles, K., Robertson, N. A., Robie, R., Robinet, F., Rocchi, A., Rolland, L., Rollins, J. G., Roma, V. J., Romano, R., Romanov, G., Romie, J. H., Rosińska, D., Röver, C., Rowan, S., Rüdiger, A., Ruggi, P., Ryan, K., Sachdev, S., Sadecki, T., Sadeghian, L., Salconi, L., Saleem, M., Salemi, F., Samajdar, A., Sammut, L., Sanchez, E. J., Sandberg, V., Sandeen, B., Sanders, J. R., Sassolas, B., Sathyaprakash, B. S., Saulson, P. R., Sauter, O., Savage, R. L., Sawadsky, A., Schale, P., Schilling, R., Schmidt, J., Schmidt, P., Schnabel, R., Schofield, R. M. S., Schönbeck, A., Schreiber, E., Schuette, D., Schutz, B. F., Scott, J., Scott, S. M., Sellers, D., Sengupta, A. S., Sentenac, D., Sequino, V., Sergeev, A., Serna, G., Setyawati, Y., Sevigny, A., Shaddock, D. A., Shah, S., Shahriar, M. S., Shaltev, M., Shao, Z., Shapiro, B., Shawhan, P., Sheperd, A., Shoemaker, D. H., Shoemaker, D. M., Siellez, K., Siemens, X., Sigg, D., Silva, A. D., Simakov, D., Singer, A., Singer, L. P., Singh, A., Singh, R., Singhal, A., Sintes, A. M., Slagmolen, B. J. J., Smith, J. R., Smith, N. D., Smith, R. J. E., Son, E. J., Sorazu, B., Sorrentino, F., Souradeep, T., Srivastava, A. K., Staley, A., Steinke, M., Steinlechner, J., Steinlechner, S., Steinmeyer, D., Stephens, B. C., Stevenson, S. P., Stone, R., Strain, K. A., Straniero, N., Stratta, G., Strauss, N. A., Strigin, S., Sturani, R., Stuver, A. L., Summerscales, T. Z., Sun, L., Sutton, P. J., Swinkels, B. L., Szczepańczyk, M. J., Tacca, M., Talukder, D., Tanner, D. B., Tápai, M., Tarabrin, S. P., Taracchini, A., Taylor, R., Theeg, T., Thirugnanasambandam, M. P., Thomas, E. G., Thomas, M., Thomas, P., Thorne, K. A., Thorne, K. S., Thrane, E., Tiwari, S., Tiwari, V., Tokmakov, K. V., Tomlinson, C., Tonelli, M., Torres, C. V., Torrie, C. I., Töyrä, D., Travasso, F., Traylor, G., Trifirò, D., Tringali, M. C., Trozzo, L., Tse, M., Turconi, M., Tuyenbayev, D., Ugolini, D., Unnikrishnan, C. S., Urban, A. L., Usman, S. A., Vahlbruch, H., Vajente, G., Valdes, G., Van Bakel, N., Van Beuzekom, M., Van Den Brand, J. F. J., Van Den Broeck, C., Vander-Hyde, D. C., Van Der Schaaf, L., Van Der Sluys, M. V., Van Heijningen, J. V., Vañó-Viñuales, A., Van Veggel, A. A., Vardaro, M., Vass, S., Vasúth, M., Vaulin, R., Vecchio, A., Vedovato, G., Veitch, J., Veitch, P. J., Venkateswara, K., Verkindt, D., Vetrano, F., Viceré, A., Vinciguerra, S., Vine, D. J., Vinet, J.-y., Vitale, S., Vo, T., Vocca, H., Vorvick, C., Voss, D., Vousden, W. D., Vyatchanin, S. P., Wade, A. R., Wade, L. E., Wade, M., Walker, M., Wallace, L., Walsh, S., Wang, G., Wang, H., Wang, M., Wang, X., Wang, Y., Ward, R. L., Warner, J., Was, M., Weaver, B., Wei, L.-w., Weinert, M., Weinstein, A. J., Weiss, R., Welborn, T., Wen, L., Weßels, P., Westphal, T., Wette, K., Whelan, J. T., White, D. J., Whiting, B. F., Williams, R. D., Williamson, A. R., Willis, J. L., Willke, B., Wimmer, M. H., Winkler, W., Wipf, C. C., Wittel, H., Woan, G., Worden, J., Wright, J. L., Wu, G., Yablon, J., Yam, W., Yamamoto, H., Yancey, C. C., Yap, M. J., Yu, H., Yvert, M., Zadrożny, A., Zangrando, L., Zanolin, M., Zendri, J.-p., Zevin, M., Zhang, F., Zhang, L., Zhang, M., Zhang, Y., Zhao, C., Zhou, M., Zhou, Z., Zhu, X. J., Zucker, M. E., Zuraw, S. E., Zweizig, J., Boyle, M., Brügmann, B., Campanelli, M., Clark, M., Hamberger, D., Kidder, L. E., Kinsey, M., Laguna, P., Ossokine, S., Scheel, M. A., Szilagyi, B., Teukolsky, S., and Zlochower, Y. (2016). Properties of the Binary Black Hole Merger GW150914. *Physical Review Letters*, 116(24).

Alvey, J., Bhardwaj, U., Domcke, V., Pieroni, M., and Weniger, C. (2024). Leveraging Time-Dependent Instrumental Noise for LISA SGWB Analysis. arXiv:2408.00832 [astro-ph, physics:gr-qc, physics:hep-ph].

Arzoumanian, Z., Baker, P. T., Blumer, H., Bécsy, B., Brazier, A., Brook, P. R., Burke-Spolaor, S., Chatterjee, S., Chen, S., Cordes, J. M., Cornish, N. J., Crawford, F., Cromartie, H. T., DeCesar, M. E., Demorest, P. B., Dolch, T., Ellis, J. A., Ferrara, E. C., Fiore, W., Fonseca, E., Garver-Daniels, N., Gentile, P. A., Good, D. C., Hazboun, J. S., Holgado, A. M., Islo, K., Jennings, R. J., Jones, M. L., Kaiser, A. R., Kaplan, D. L., Kelley, L. Z., Key, J. S., Laal, N., Lam, M. T., W. Lazio, T. J., Lorimer, D. R., Luo, J., Lynch, R. S., Madison, D. R., McLaughlin, M. A., Mingarelli, C. M. F., Ng, C., Nice, D. J., Pennucci, T. T., Pol, N. S., Ransom, S. M., Ray, P. S., Shapiro-Albert, B. J., Siemens, X., Simon, J., Spiewak, R., Stairs, I. H., Stinebring, D. R., Stovall, K., Sun, J. P., Swiggum, J. K., Taylor, S. R., Turner, J. E., Vallisneri, M., Vigeland, S. J., Witt, C. A., and The NANOGrav Collaboration (2020). The NANOGrav 12.5 yr Data Set: Search for an Isotropic Stochastic Gravitational-wave Background. *ApJL*, 905(2):L34.

Barish, B. C. and Weiss, R. (1999). LIGO and the Detection of Gravitational Waves. *Physics Today*, 52(10):44–50.

Bayle, J.-B. (2019). *Simulation and Data Analysis for LISA (Instrumental Modeling, Time-Delay Interferometry, Noise-Reduction Performance Study, and Discrimination of Transient Gravitational Signals)*. Theses, Université de Paris ; Université Paris Diderot ; Laboratoire Astroparticules et Cosmologie.

Bayle, J.-B. and Hartwig, O. (2023). Unified model for the LISA measurements and instrument simulations. *Phys. Rev. D*, 107(8):083019.

Buscicchio, R., Klein, A., Korol, V., Renzo, F. D., Moore, C. J., Gerosa, D., and Carzaniga, A. (2024). A test for LISA foreground Gaussianity and stationarity. I. Galactic white-dwarf binaries. arXiv:2410.08263 [astro-ph].

Cireddu, F., Wils, M., Wong, I. C. F., Pang, P. T. H., Li, T. G. F., and Pozzo, W. D. (2024). Likelihood for a Network of Gravitational-Wave Detectors with Correlated Noise. arXiv:2312.14614 [gr-qc].

Colpi, M., Danzmann, K., Hewitson, M., Holley-Bockelmann, K., Jetzer, P., Nelemans, G., Petiteau, A., Shoemaker, D., Sopuerta, C., Stebbins, R., Tanvir, N., Ward, H., Weber, W. J., Thorpe, I., Daurskikh, A., Deep, A., Núñez, I. F., Marirrodriga, C. G., Gehler, M., Halain, J.-P., Jennrich, O., Lammers, U., Larrañaga, J., Lieser, M., Lützgendorf, N., Martens, W., Mondin, L., Niño, A. P., Amaro-Seoane, P., Sedda, M. A., Auclair, P., Babak, S., Baghi, Q., Baibhav, V., Baker, T., Bayle, J.-B., Berry, C., Berti, E., Boileau, G., Bonetti, M., Brito, R., Buscicchio, R., Calcagni, G., Capelo, P. R., Caprini, C., Caputo, A., Castelli, E., Chen, H.-Y., Chen, X., Chua, A., Davies, G., Derdzinski, A., Domcke, V. F., Doneva, D., Dvorkin, I., Ezquiaga, J. M., Gair, J., Haiman, Z., Harry, I., Hartwig, O., Hees, A., Heffernan, A., Husa, S., Izquierdo, D., Karnesis, N., Klein, A., Korol, V., Korsakova, N., Kupfer, T., Laghi, D., Lamberts, A., Larson, S., Jeune, M. L., Lewicki, M., Littenberg, T., Madge, E., Mangiagli, A., Marsat, S., Vilchez, I. M., Maselli, A., Mathews, J., van de Meent, M., Muratore, M., Nardini, G., Pani, P., Peloso, M., Pieroni, M., Pound, A., Quelquejay-Leclere, H., Ricciardone, A., Rossi, E. M., Sartirana, A., Savalle, E., Sberna, L., Sesana, A., Shoemaker, D., Slutsky, J., Sotiriou, T., Speri, L., Staab, M., Steer, D., Tamanini, N., Tasinato, G., Torrado, J., Torres-Orjuela, A., Toubiana, A., Vallisneri, M., Vecchio, A., Volonteri, M., Yagi, K., and Zwick, L. (2024). LISA Definition Study Report. arXiv:2402.07571 [astro-ph, physics:gr-qc].

contributors, W. (2025). Laser Interferometer Space antenna.

De Vries, G. (2025). Saxony also wants to build the Einstein Telescope - Einstein Telescope.

ET-EMR collaboration (2025). Organisation and timeline - Einstein Telescope.

Gair, J. R., Antonelli, A., and Barbieri, R. (2022). A Fisher matrix for gravitational-wave population inference. *Monthly Notices of the Royal Astronomical Society*, 519(2):2736–2753. arXiv:2205.07893 [gr-qc].

Group, L. C. W. W., Afshordi, N., Akçay, S., Seoane, P. A., Antonelli, A., Aurrekoetxea, J. C., Barack, L., Barausse, E., Benkel, R., Bernard, L., Bernuzzi, S., Berti, E., Bonetti, M., Bonga, B., Bozzola, G., Brito, R., Buonanno, A., Cárdenas-Avendaño, A., Casals, M., Chernoff, D. F., Chua, A. J. K., Clough, K., Colleoni, M., Dhesi, M., Druart, A., Durkan, L., Faye, G., Ferguson, D., Field, S. E., Gabella, W. E., García-Bellido, J., Gracia-Linares, M., Gerosa, D., Green, S. R., Haney, M., Hannam, M., Heffernan, A., Hinderer, T., Helfer, T., Hughes, S. A., Husa, S., Isoyama, S., Katz, M. L., Kavanagh, C., Khanna, G., Kidder, L. E., Korol, V., Küchler, L., Laguna, P., Larrouturou, F., Tiec, A. L., Leather, B., Lim, E. A., Lim, H., Littenberg, T. B., Long, O., Lousto, C. O., Lovelace, G., Lukes-Gerakopoulos, G., Lynch, P., Macedo, R. P., Markakis, C., Maggio, E., Mandel, I., Maselli, A., Mathews, J., Mourier, P., Neilsen, D., Nagar, A., Nichols, D. A., Novák, J., Okounkova, M., O'Shaughnessy, R., Oshita, N., O'Toole, C., Pan, Z., Pani, P., Pappas, G., Paschalidis, V., Pfeiffer, H. P., Pompili, L., Pound, A., Pratten, G., Rüter, H. R., Ruiz, M., Sam, Z., Sberna, L., Shapiro, S. L., Shoemaker, D. M., Sopuerta, C. F., Spiers, A., Sundar, H., Tamanini, N., Thompson, J. E., Toubiana, A., Tsokaros, A., Upton, S. D., van de Meent, M., Vernieri, D., Wachter, J. M., Warburton, N., Wardell, B., Witek, H., Witzany, V., Yang, H., Zilhão, M., Albertini, A., Arun, K. G., Bezares, M., Bonilla, A., Chapman-Bird, C., Cownden, B., Cunningham, K., Devitt, C., Dolan, S., Duque, F., Dyson, C., Fryer, C. L., Gair, J. R., Giacomazzo, B., Gupta, P., Han, W.-B., Haas, R., Hirschmann, E. W., Huerta, E. A., Jetzer, P., Kelly, B., Khalil, M., Lewis, J., Lloyd-Ronning, N., Marsat, S., Nardini, G., Neef, J., Ottewill, A., Pantelidou, C., Piovano, G. A., Redondo-Yuste, J., Sagunski, L., Stein, L. C., Skoupý, V., Sperhake, U., Speri, L., Spieksma, T. F. M., Stevens, C., Trestini, D., and Vañó-Viñuales, A. (2023). Waveform Modelling for the Laser Interferometer Space Antenna. arXiv:2311.01300 [astro-ph, physics:gr-qc].

Hartwig, O., Lilley, M., Muratore, M., and Pieroni, M. (2023). Stochastic gravitational wave background reconstruction for a non-equilateral and unequal-noise LISA constellation. *Phys. Rev. D*, 107(12):123531. arXiv:2303.15929 [astro-ph, physics:gr-qc].

Hartwig, O. and Muratore, M. (2022). Characterization of Time Delay Interferometry combinations for the LISA instrument noise. *Phys. Rev. D*, 105(6):062006. arXiv:2111.00975 [gr-qc].

JAX authors (2025a). Errors — JAX documentation.

JAX authors (2025b). Quickstart — JAX documentation.

Katz, M. L., Bayle, J.-B., Chua, A. J. K., and Vallisneri, M. (2022). Assessing the data-analysis impact of LISA orbit approximations using a GPU-accelerated response model. *Phys. Rev. D*, 106(10):103001. arXiv:2204.06633 [astro-ph, physics:gr-qc].

Katz, M. L., Chua, A. J. K., Speri, L., Warburton, N., and Hughes, S. A. (2021). FastEMRIWaveforms: New tools for millihertz gravitational-wave data analysis. *Phys. Rev. D*, 104(6):064047. arXiv:2104.04582 [gr-qc].

Katz, M. L., Karnesis, N., Korsakova, N., Gair, J. R., and Stergioulas, N. (2024). An efficient GPU-accelerated multi-source global fit pipeline for LISA data analysis. arXiv:2405.04690 [gr-qc].

Legin, R., Adam, A., Hezaveh, Y., and Levasseur, L. P. (2023). Beyond Gaussian Noise: A Generalized Approach to Likelihood Analysis with non-Gaussian Noise. *ApJL*, 949(2):L41. arXiv:2302.03046 [astro-ph].

Li, E.-K., Liu, S., Torres-Orjuela, A., Chen, X., Inayoshi, K., Wang, L., Hu, Y.-M., Amaro-Seoane, P., Askar, A., Bambi, C., Capelo, P. R., Chen, H.-Y., Chua, A. J. K., Condés-Breña, E., Dai, L., Das, D., Derdzinski, A., Fan, H.-M., Fujii, M., Gao, J., Garg, M., Ge, H., Giersz, M., Huang, S.-J., Hypki, A., Liang, Z.-C., Liu, B., Liu, D., Liu, M., Liu, Y., Mayer, L., Napolitano, N. R., Peng, P., Shao, Y., Shashank, S., Shen, R., Tagawa, H., Tanikawa, A., Toscani, M., Vázquez-Aceves, V., Wang, H.-T., Wang, H., Yi, S.-X., Zhang, J.-d., Zhang, X.-T., Zhu, L., Zwick, L., Huang, S., Mei, J., Wang, Y., Xie, Y., Zhang, J., and Luo, J. (2024). Gravitational Wave Astronomy With TianQin. arXiv:2409.19665 [astro-ph].

Li, T. G. F. (2024). *Notes on Gravitational Waves*.

Luo, Z., Guo, Z., Jin, G., Wu, Y., and Hu, W. (2020). A brief analysis to Taiji: Science and technology. *Results in Physics*, 16:102918.

Maggiore, M. (2017). *Gravitational waves*. Oxford university press, Oxford.

Moore, C. J., Cole, R. H., and Berry, C. P. L. (2014). Gravitational-wave sensitivity curves. *Classical and Quantum Gravity*, 32(1):015014.

Nobel Prize committee (2017). Nobel prize in physics 2017.

Ross, S. M. (2019). *Introduction to probability models*. Academic Press.

Schutz, B. F. (1986). Determining the Hubble constant from gravitational wave observations. *Nature*, 323(6086):310–311.

Tinto, M. and Dhurandhar, S. V. (2021). Time-delay interferometry. *Living Rev Relativ*, 24(1):1.

Wikipedia contributors (2025a). Complex normal distribution.

Wikipedia contributors (2025b). Hamiltonian Monte Carlo.

Wikipedia contributors (2025c). LIGO.

Wong, I. C. F., Pang, P. T. H., Wils, M., Cireddu, F., Del Pozzo, W., and Li, T. G. F. (2024). The Potential Impact of Noise Correlation in Next-generation Gravitational Wave Detectors. arXiv:2407.08728 [astro-ph, physics:gr-qc].

Wong, K. W. K., Isi, M., and Edwards, T. D. P. (2023). Fast gravitational wave parameter estimation without compromises. arXiv:2302.05333 [astro-ph, physics:gr-qc].

Wouters, T., Pang, P. T. H., Dietrich, T., and Broeck, C. V. D. (2024). Robust parameter estimation within minutes on gravitational wave signals from binary neutron star inspirals. arXiv:2404.11397 [astro-ph, physics:gr-qc].

Appendices

Appendix A

Addendum on the noise modelling

A.1 Deriving the LISA PSDs and CSDs

Let us start with the definition of Power Spectral Density and Cross Power Spectral Density. For detectors k and l in a network of N detectors, their PSD and CSD are given by:

$$< \tilde{n}_k^\dagger(f)\tilde{n}_l(f') >\equiv \delta(f-f')\frac{1}{2}S_{kl}(f) \tag{A.1}$$

For LISA, we have 6 single-link phase detectors, which will be noted as S_{ij} for a single-link shot from satellite i and received in satellite j. In literature, the two main noise sources identified for these single-link detectors are the Test Mass (TM) and Optical Metrology Systems (OMS) noise and are modelled as the following in the literature (e.g. Hartwig et al. (2023); Alvey et al. (2024)):

$$S_{ij}^{\mathrm{TM}}(f) = 10^{-30}\times A_{ij}^2 \times \left(1+\left(\frac{0.4\mathrm{mHz}}{f}\right)^2\right)\times\left(1+\left(\frac{f}{8\mathrm{mHz}}\right)^4\right)\times(2\pi f c)^{-2}\times \mathrm{m^2s^{-3}}, \tag{A.2}$$

$$S_{ij}^{\mathrm{OMS}}(f) = 10^{-24}\times P_{ij}^2\times\left(1+\left(\frac{2\mathrm{mHz}}{f}\right)^4\right)\times\left(\frac{2\pi f}{c}\right)^2\times\mathrm{m^2Hz^{-1}}, \tag{A.3}$$

where A_{ij} and P_{ij} are dimensionless detector-specific parameters and c is light speed. Furthermore, we can then identify the full noise contribution in the measurement (in the time domain):(?)

$$\begin{aligned} n_{ij}(t) &= n_{ij}^{\mathrm{TM}}(t) + n_{ij}^{\mathrm{OMS}}(t) + \mathcal{D}_{ij}[n_{ij}^{\mathrm{TM}}](t), \\ &= n_{ij}^{\mathrm{TM}}(t) + n_{ij}^{\mathrm{OMS}}(t) + n_{ij}^{\mathrm{TM}}(t-L_{ij}(t)). \end{aligned} \tag{A.4}$$

Here, we call $\mathcal{D}_{ij}$ the delay operator, which delays the noise (in the time domain) by the time-dependent armlength $L_{ij}(t)$ (using coordinates where $c=1$). In order to generate the PSDs, and CSDs in the frequency domain, the change of the armlength across time needs to be specified. However, if the assumption is made that the armlengths are roughly constant across time, the delay operator's contributions the noise terms contributes to a factor $\exp(-2\pi i f L_{ij})$ in the frequency domain.[1] Through some simple algebra using equation (A.4), we find that

[1]This can easily be seen through the following identity:

$$(\widetilde{\mathcal{D}_{ij}[y]})(f) = \int \mathcal{D}_{ij}y(t)e^{-2\pi i f t}\mathrm{d}t = \int y(t-L_{ij})e^{-2\pi i f t}\mathrm{d}t = e^{-2\pi i f L_{ij}}\tilde{y}(f)$$

these noise terms then have the following (cross-)power spectral densities:

$$S_{ij,ij} = S_{ij}^{\text{OMS}} + S_{ij}^{\text{TM}} + S_{ji}^{\text{TM}}, \tag{A.5}$$

$$S_{ij,ji} = e^{2\pi i f L_{ji}} S_{ij}^{\text{TM}} + e^{-2\pi i f L_{ij}} S_{ji}^{\text{TM}}. \tag{A.6}$$

Note how this is only accurate for constant (though not necessarily equal) armlengths ($L_{ij}(t) = L_{ij}$). If the armlengths are allowed to vary by time, the orbit function needs to be specified.

Sampling noise

When generating the noise samples from a given PSD or covariance matrix $\mathbf{S}(f)$, it is assumed the (complex) noise is gaussian and therefore follow a circularly symmetric comlex normal distribution in the frequency space. More exactly, for digital signals with frequency resolution Δf the noise at frequency f_k is sampled from the following distribution:(Wikipedia contributors (2025a))

$$(\text{Re}[\tilde{\mathbf{n}}(f_k)], \text{Im}[\tilde{\mathbf{n}}(f_k)]) \sim \mathcal{N}\left((\mathbf{0}, \mathbf{0}); 2\Delta f \begin{bmatrix} \text{Re}[\mathbf{S}(f_k)] & -\text{Im}[\mathbf{S}(f_k)] \\ \text{Im}[\mathbf{S}(f_k)] & \text{Re}[\mathbf{S}(f_k)] \end{bmatrix}\right). \tag{A.7}$$

However, for fully symmetric noise models, the CSD becomes real and therefore the real and imaginary parts become uncorrelated. This in turn simplifies the noise sampling to merely sampling from the same multivariate normal distribution:

$$\text{Re}[\tilde{\mathbf{n}}(f_k)], \text{Im}[\tilde{\mathbf{n}}(f_k)] \sim \mathcal{N}(\mathbf{0}; \mathbf{S}(f_k)). \tag{A.8}$$

As triangular ET is currently expected to have real CSDs, this simplified form is used when creating mock data.(Cireddu et al. (2024))

A.2 Michelson Variables (XYZ)

Let us restate the Michelson variables, described as the following sum of phase measurements and delay operators:

$$X = (1 - \mathcal{D}_{13}\mathcal{D}_{31})[y_{12} + \mathcal{D}_{12}[y_{21}]] - (1 - \mathcal{D}_{12}\mathcal{D}_{21})[y_{13} + \mathcal{D}_{13}[y_{31}]]. \tag{A.9}$$

We can find the other detectors Y and Z by performing cycle substitutions between $(XYZ) \longleftrightarrow (123)$. Physically, we can interpret each term as the phase difference of the arriving and returning EM waves for each arm. The difference of these terms is then clearly the kind of phase measurement that would be made by a Michelson interferometer with constant arms. We can then verify that this physically represents the phase measurement of a would-be Michelson interferometer.

Let us now derive the relevant PSDs and CSDs. Assuming constant arms, we can find that the data streams for the $X-$ and the $Y-$channel in the frequency domain become:

$$\tilde{X} = (1 - e^{-2\pi i f(L_{13}+L_{31})})(\tilde{y}_{12} + e^{-2\pi i L_{12}}\tilde{y}_{21}) - (1 - e^{-2\pi i f(L_{12}+L_{21})})(\tilde{y}_{13} + e^{-2\pi i f L_{13}}\tilde{y}_{31}). \tag{A.10}$$

$$\tilde{Y} = (1 - e^{-2\pi i f(L_{21}+L_{12})})(\tilde{y}_{23} + e^{-2\pi i L_{23}}\tilde{y}_{32}) - (1 - e^{-2\pi i f(L_{23}+L_{32})})(\tilde{y}_{21} + e^{-2\pi i f L_{21}}\tilde{y}_{12}). \tag{A.11}$$

We can further make our calculations easier when assessing the PSDs and CSDs by noting the fact that $< n_{ij}|n_{kl} >\neq 0$ only if $ij = kl$ or $ij = lk$. Using this identity and equations (A.5), (A.6) and (A.10), our $X-$channel's PSD S^{XX} then becomes

$$
\begin{aligned}
S^{XX} &= |1-e^{-2\pi if(L_{13}+L_{31})}|^2(S_{12,12}+S_{21,21}+e^{-2\pi iL_{12}}S_{12,21}+e^{2\pi ifL_{12}}S_{21,12}) \quad \text{(A.12a)}\\
&+|1-e^{-2\pi if(L_{13}+L_{31})}|^2(S_{13,13}+S_{31,31}+e^{-2\pi ifL_{13}}S_{13,31}+e^{2\pi iL_{13}}S_{31,13}),\\
&=4\sin^2[\pi(L_{12}+L_{21})](S_{12}^{\mathrm{OMS}}+S_{21}^{\mathrm{OMS}}+2S_{12}^{\mathrm{TM}}+2S_{21}^{\mathrm{TM}}\\
&+e^{2\pi if(L_{21}-L_{12})}S_{12}^{\mathrm{TM}}+e^{-4\pi ifL_{12}}S_{21}^{\mathrm{TM}}+e^{-2\pi if(L_{21}-L_{12})}S_{12}^{\mathrm{TM}}+e^{4\pi iL_{12}}S_{21}^{\mathrm{TM}}) \quad \text{(A.12b)}\\
&+4\sin^2[\pi f(L_{13}+L_{31})](S_{13}^{\mathrm{OMS}}+S_{31}^{\mathrm{OMS}}+2S_{13}^{\mathrm{TM}}+2S_{31}^{\mathrm{TM}}\\
&+e^{2\pi if(L_{31}-L_{13})}S_{13}^{\mathrm{TM}}+e^{-4\pi ifL_{13}}S_{31}^{\mathrm{TM}}+e^{-2\pi i(L_{31}-L_{13})}S_{13}^{\mathrm{TM}}+e^{4\pi ifL_{13}}S_{31}^{\mathrm{TM}}),\\
&=4\sin^2[\pi f(L_{12}+L_{21})](S_{12}^{\mathrm{OMS}}+S_{21}^{\mathrm{OMS}}+4\cos^2[\pi f(L_{12}-L_{21})]S_{12}^{\mathrm{TM}}+4\cos^2[\pi f(L_{12}+L_{21})])S_{21}^{\mathrm{TM}})\\
&+4\sin^2[\pi f(L_{13}+L_{31})](S_{13}^{\mathrm{OMS}}+S_{31}^{\mathrm{OMS}}+4\cos^2[\pi f(L_{13}-L_{31})]S_{13}^{\mathrm{TM}}+4\cos^2[\pi f(L_{13}+L_{31})])S_{31}^{\mathrm{TM}}).
\end{aligned}
\tag{A.12c}
$$

This last expression can then finally be simplified in the fully symmetric case (i.e. when $L_{ij} = L, S_{ij}^{\mathrm{TM}} = S^{\mathrm{TM}}$, and $S_{ij}^{\mathrm{OMS}} = S^{\mathrm{OMS}}$) to the following equation:(Hartwig et al. (2023))

$$S^{XX} = 16\sin^2(2\pi fL)(S^{\mathrm{OMS}}+(3+\cos(4\pi fL))S_{21}^{\mathrm{TM}}). \tag{A.13}$$

We can also make a slightly weaker approximation that is commonly used across the literature: assuming that the armlength in each direction is equal. More exactly, $L_{ij} = L_{ji}$ for all detectors ij (while still assuming $S_{ij}^{\mathrm{OMS,TM}} \neq S_{ji}^{\mathrm{OMS,TM}}$). Using this approximation on top of the constant arm approximation, we can reduce (A.12) to

$$
\begin{aligned}
S^{XX} &= 4\sin^2[2\pi fL_{12}](S_{12}^{\mathrm{OMS}}+S_{21}^{\mathrm{OMS}}+4S_{12}^{\mathrm{TM}}+4\cos^2[2\pi fL_{12}]S_{21}^{\mathrm{TM}})\\
&+4\sin^2[2\pi fL_{13}](S_{13}^{\mathrm{OMS}}+S_{31}^{\mathrm{OMS}}+4S_{13}^{\mathrm{TM}}+4\cos^2[2\pi fL_{13}]S_{31}^{\mathrm{TM}}).
\end{aligned}
\tag{A.14}
$$

Next, we can analogously find the off-diagonal term S^{XY}. Luckily, the only relevant terms are the ones containing $\tilde{n}_{12}$ and $\tilde{n}_{21}$. Applying the same principles and techniques, we derive our expression for S^{XY}:

$$
\begin{aligned}
S^{XY} &= -(1-e^{2\pi if(L_{13}+L_{31})})(1-e^{-2\pi if(L_{23}+L_{32})})(S_{12,21}+e^{2\pi if(L_{12}-L_{21})}S_{21,12} \quad \text{(A.15a)}\\
&+e^{-2\pi iL_{21}}S_{12,12}+e^{2\pi iL_{12}}S_{21,21}),\\
&=-(1-e^{2\pi if(L_{13}+L_{31})}-e^{-2\pi if(L_{23}+L_{32})}+e^{2\pi if(L_{13}+L_{31}-L_{23}-L_{32})})\\
&\times(e^{-2\pi ifL_{21}}S_{21}^{\mathrm{OMS}}+[2\cos(2\pi fL_{12})+e^{2\pi ifL_{12}}+e^{2\pi if(L_{21}-2L_{12})}]S_{21}^{\mathrm{TM}}\\
&+e^{2\pi ifL_{12}}S_{12}^{\mathrm{OMS}}+[2\cos(2\pi fL_{12})+e^{2\pi ifL_{12}}+e^{-2\pi ifL_{21}}]S_{12}^{\mathrm{TM}}).
\end{aligned}
\tag{A.15b}
$$

We can further find simplified versions of this equation through the same assumptions of symmetry. For the fully symmetric case, we find the following cross term:

$$S^{XY} = -4\sin(2\pi fL)\sin(4\pi fL)(S^{\mathrm{OMS}}+4S^{\mathrm{TM}}). \tag{A.16}$$

Similarly to (A.14), we can find the same type of result under the same approximations:

$$
\begin{aligned}
S^{XY} &= -(1-e^{4\pi ifL_{13}}-e^{-4\pi ifL_{23}}+e^{4\pi if(L_{13}-L_{23})})\\
&\times(e^{-2\pi ifL_{21}}S_{21}^{\mathrm{OMS}}+e^{2\pi ifL_{12}}S_{12}^{\mathrm{OMS}}+4\cos(2\pi fL_{12})(S_{21}^{\mathrm{TM}}+S_{12}^{\mathrm{TM}})).
\end{aligned}
\tag{A.17}
$$

Finally, we also note the TDI-2 versions for Michelson vairables (XYZ), which are used to reduce the shot noise below secondary noise levels. Since multiple candidates exist to suppress this noise, we state an often-used one, following (Hartwig et al. (2023)):

$$X_2 = (1 - \mathcal{D}_{31}^2\mathcal{D}_{12}^2)X. \tag{A.18}$$

Due to the fact the second generation TDI variables are only useful when the armlengths are both non-equal and varying in time, no simple or elegant PSD or CSD has been provided as they would also be dependent on the orbit.

A.3 Sagnac Variables ($\alpha\beta\gamma\zeta$)

The Sagnac variables are written in function of the single links the following fashion:Tinto and Dhurandhar (2021)

$$\alpha = (y_{12} + \mathcal{D}_{12}y_{23} + \mathcal{D}_{12}\mathcal{D}_{23}y_{31}) - (y_{13} + \mathcal{D}_{13}y_{32} + \mathcal{D}_{13}\mathcal{D}_{32}y_{23}), \tag{A.19}$$
$$\zeta = \mathcal{D}_{12}(y_{31} - y_{32}) + \mathcal{D}_{23}(y_{12} - y_{13}) + \mathcal{D}_{31}(y_{23} - y_{21}). \tag{A.20}$$

Analogous to the Michelson variables, one can also write the β and γ channels through cyclic permutation with α. It is also analogously easy to physically interpret for the reader as the clockwise laser stream (the first term in (A.19)) interfering with the corresponding counterclockwise laser stream (the second term in (A.19)). ζ itself is not fully independent of the other Sagnac variables as it can be related to the other channels via the following relation:

$$(1 - \mathcal{D}_{23}\mathcal{D}_{31}\mathcal{D}_{12})\zeta = (\mathcal{D}_{23} - \mathcal{D}_{31}\mathcal{D}_{12})\alpha + (\mathcal{D}_{31} - \mathcal{D}_{23}\mathcal{D}_{12})\beta + (\mathcal{D}_{12} - \mathcal{D}_{23}\mathcal{D}_{31})\gamma. \tag{A.21}$$

It has been shown that any other set of TDI variables can be generated by a set of 4 generators, such as $\{\alpha, \beta, \gamma, \zeta\}$.(Hartwig et al. (2023)) Similarly to the Michelson variables, the corresponding PSDs and CSDs can be calculated. This will be left as an exercise to the reader and only the fully symmetric case with equal armlengths will be provided:

$$S^{\alpha\alpha} = 6S^{\mathrm{OMS}} + 4(3 - 2\cos(2\pi fL) - \cos(6\pi fL))S^{\mathrm{TM}}, \tag{A.22}$$
$$S^{\alpha\beta} = 2(\cos(4\pi fL) + 2\cos(2\pi fL))S^{\mathrm{OMS}} + 4(1 - \cos(2\pi fL))S^{\mathrm{TM}}, \tag{A.23}$$
$$S^{\zeta\zeta} = 6S^{\mathrm{OMS}} + 12(1 - \cos(2\pi fL))S^{\mathrm{TM}}, \tag{A.24}$$
$$S^{\alpha\zeta} = 0. \tag{A.25}$$

Finally, TDI-2 variants of the Sagnac variables have been proposed in order to take the armlength variation into account. Such a possible, often-used choice for α and ζ is

$$\alpha_2 = (1 - \mathcal{D}_{12}\mathcal{D}_{23}\mathcal{D}_{31})\alpha, \tag{A.26}$$
$$\zeta_2 = (\mathcal{D}_{31} - \mathcal{D}_{12}\mathcal{D}_{23})\zeta. \tag{A.27}$$

A.4 Diagonalisation through the (AET) base

Assuming full symmetry between all detectors (i.e. $A_{ij} = A_{kl}$, $P_{ij} = P_{kl}$, $L_{ij}(t) = L_{kl}(t) \implies \mathcal{D}_{ij}(t) = \mathcal{D}_{jk}(t)$ for all detectors ij and kl), it can be argued through symmetry that the covariance matrix for both for both the Michelson variables (XYZ) and the Sagnac variables ($\alpha\beta\gamma$) will have the following form:

$$\mathbf{S}(f) = \begin{pmatrix} D & C & C \\ C & D & C \\ C & C & D \end{pmatrix}(f). \tag{A.28}$$

After a brief analysis and applying our knowledge of linear algebra, one can find that this covariance matrix has a convenient orthogonal base transformation to make it a diagonal matrix with eigenvalues $\mu_A = \mu_E = D - C$ and $\mu_T = D + 2C$ and corresponding orthonormal eigenvectors:

$$\begin{aligned} \mathbf{e}_A &= \frac{\mathbf{e}_3 - \mathbf{e}_1}{\sqrt{2}}, \\ \mathbf{e}_E &= \frac{\mathbf{e}_1 - 2\mathbf{e}_2 + \mathbf{e}_3}{\sqrt{6}}, \\ \mathbf{e}_T &= \frac{\mathbf{e}_1 + \mathbf{e}_2 + \mathbf{e}_3}{\sqrt{3}}, \end{aligned} \tag{A.29}$$

with $\mathbf{e}_k \in \{\mathbf{e}_X, \mathbf{e}_Y, \mathbf{e}_Z\}$ or $\{\mathbf{e}\alpha, \mathbf{e}_\beta, \mathbf{e}_\gamma\}$ depending on your choice of variables.[2] This coordinate transformation thus allows us simplify our inner product for $< s|h >$ to the following expression

$$\begin{aligned} (\mathbf{s}|\mathbf{h}) &\equiv \mathrm{Re}\left[\int \tilde{\mathbf{s}}^\dagger \left(\mathbf{S}^{-1}\right) \tilde{\mathbf{h}} \mathrm{d}f\right], \qquad \text{(A.30)} \\ &= \mathrm{Re}\left[\int \frac{\tilde{s}_A^\dagger \tilde{h}_A}{D(f) - C(f)} \mathrm{d}f\right] + \mathrm{Re}\left[\int \frac{\tilde{s}_E^\dagger \tilde{h}_E}{D(f) - C(f)} \mathrm{d}f\right] + \mathrm{Re}\left[\int \frac{\tilde{s}_T^\dagger \tilde{h}_T}{D(f) + 2C(f)} \mathrm{d}f\right] \end{aligned}$$

As one can see from the above equation, this base transformation turns our inner product from a sum of 6 terms with an otherwise undetermined inverse for the covariance to a sum of 3 easier integrals, which is why it is a popular choice in literature for analysis as it simplifies the likelihood functions.

Since there are several cases where the off-diagonal terms in the AET base are actually non-zero (e.g. when taking unequal noise into account or when the stochastic gravitational wave background is modelled as gaussian noise), it might also be relevant to note the coordinate transformation for the covariance matrix in general. For a matrix $\mathbf{S}$ of the form

$$\mathbf{S} = \begin{pmatrix} S^{11} & S^{12} & S^{13} \\ (S^{12})^\dagger & S^{22} & S^{23} \\ (S^{13})^\dagger & (S^{23})^\dagger & S^{33} \end{pmatrix}, \tag{A.31}$$

[2]Even though the choice of order for $\mathbf{e}_k$ is arbitrary due to symmetry in their noise, the convention is to pick $\mathbf{e}_1 = \mathbf{e}_X$, $\mathbf{e}_2 = \mathbf{e}_Y$ and $\mathbf{e}_3 = \mathbf{e}_Z$ for the Michelson variables and $\mathbf{e}_1 = \mathbf{e}_\alpha$, $\mathbf{e}_2 = \mathbf{e}_\beta$ and $\mathbf{e}_3 = \mathbf{e}_\gamma$.

we find their elements in the AET base to be:

$$
\begin{aligned}
S^{AA} &= \frac{S^{33} + S^{11} - 2\mathrm{Re}\,[S^{13}]}{2}, \\
S^{EE} &= \frac{S^{33} + S^{11} - \mathrm{Re}\,[2S^{12} + 2S^{23} - S^{23}]}{6}, \\
S^{TT} &= \frac{S^{11} + S^{22} + S^{33} + 2\mathrm{Re}\,[S^{12} + S^{13} + S^{23}]}{3}, \\
S^{AE} &= \frac{2(S^{23})^{\dagger} - 2S^{12} - S^{11} + S^{33} + 2i\mathrm{Im}\,[S^{13}]}{2\sqrt{3}}, \\
S^{AT} &= \frac{S^{33} - S^{11} + S^{13} - (S^{12})^{\dagger} + S^{23} + 2i\mathrm{Im}\,[S^{13}]}{\sqrt{6}}, \\
S^{ET} &= \frac{S^{11} + S^{33} - 2S^{22} + 2\mathrm{Re}\,[S^{13}] + S^{12} + (S^{23})^{\dagger} - 2S^{23} - 2(S^{12})^{\dagger}}{3\sqrt{2}}.
\end{aligned}
\tag{A.32}
$$

Appendix B

Miscellaneous figures

In this appendix the covariance graphs for the Michelson variables (XYZ) and the quasi-orthogonal variables (AET) are provided, both with symmetric noise and asymmetric noise (indicated with a subscript $\neq$). Note that since the CSD is non-real in the asymmetric case, the absolute value is shown. One more interesting thing to note is that since the (AET) variables were created to elimate the CSDs, the off-diagonals for the symmetric (AET) noise model are always 0 and therefore not visible in the log-log plot.

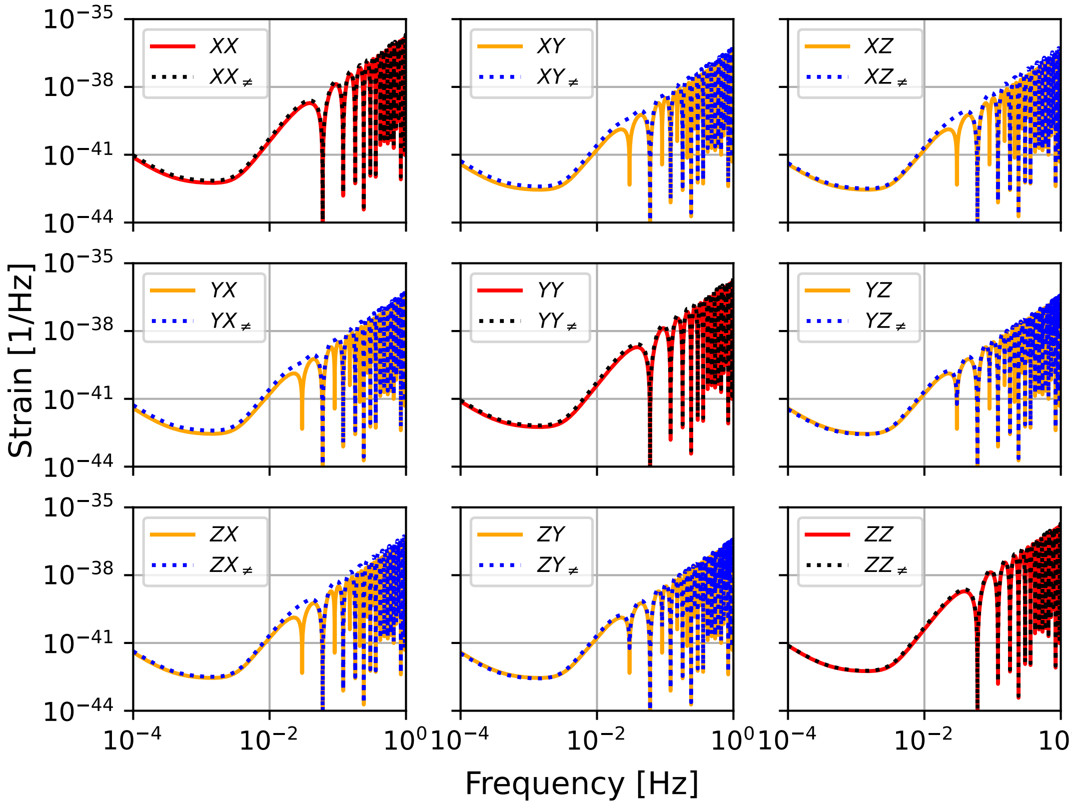

Figure B.1: LISA PSD (noted as XX, YY, and ZZ) and CSD (noted as XY, YZ, ZX etc.) graphs for the Michelson variables XYZ.

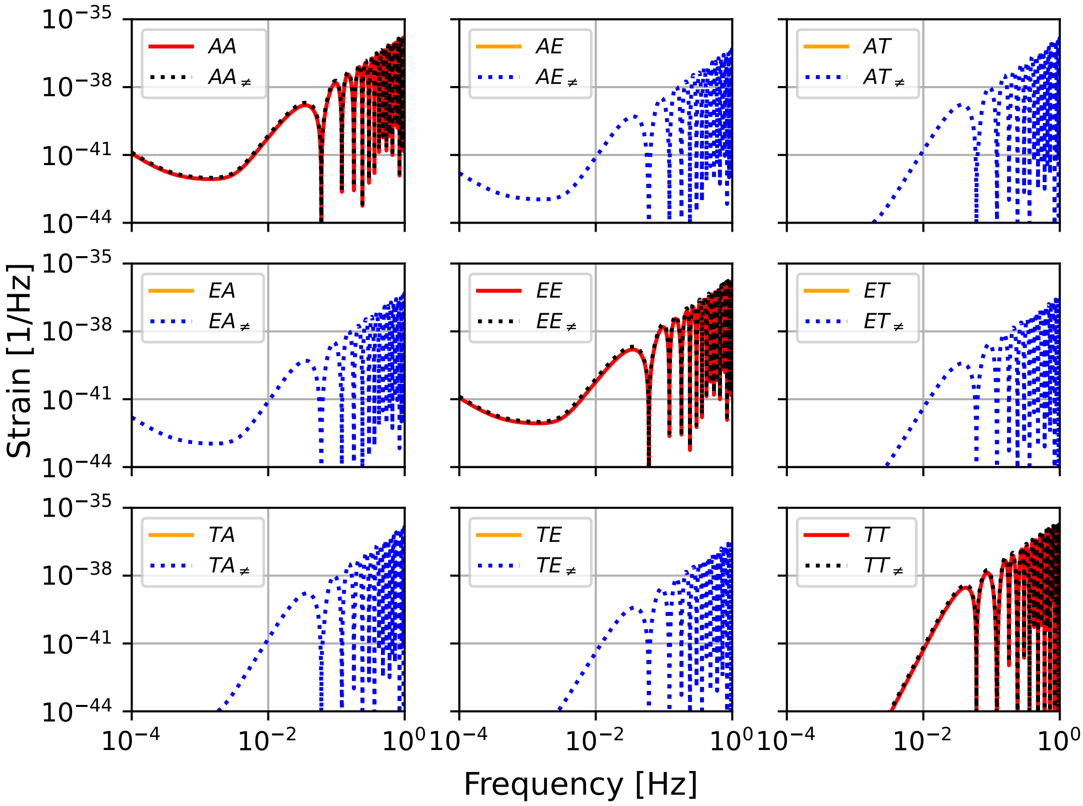

Figure B.2: LISA PSD (noted as AA, EE, and TT) and CSD (noted as AE, ET, TA etc.) plots for the quasi-orthogonal variables AET.

AFDELING
Straat nr bus 0000
3000 LEUVEN, BELGIË
tel. + 32 16 00 00 00
fax + 32 16 00 00 00
www.kuleuven.be